



Mutual Coupling-Aware Localization for RIS-Assisted ISAC Systems

Downloaded from: <https://research.chalmers.se>, 2025-05-12 03:06 UTC

Citation for the original published paper (version of record):

Fadakar, A., Keskin, M., Chen, H. et al (2025). Mutual Coupling-Aware Localization for RIS-Assisted ISAC Systems. IEEE Transactions on Cognitive Communications and Networking, In Press. <http://dx.doi.org/10.1109/TCCN.2025.3565541>

N.B. When citing this work, cite the original published paper.

© 2025 IEEE. Personal use of this material is permitted. Permission from IEEE must be obtained for all other uses, in any current or future media, including reprinting/republishing this material for advertising or promotional purposes, or reuse of any copyrighted component of this work in other works.

Mutual Coupling-Aware Localization for RIS-Assisted ISAC Systems

Alireza Fadakar, *Graduate Student Member, IEEE*, Musa Furkan Keskin, *Member, IEEE*, Hui Chen, *Member, IEEE*, and Henk Wymeersch, *Fellow, IEEE*

Abstract—Integrated sensing and communication (ISAC) is recognized as a promising approach to address the growing spectrum requirements for seamless sensing and communication. This paper investigates the deployment of reconfigurable intelligent surface (RIS) in ISAC systems under line-of-sight (LoS) obstructions, addressing the limited attention given to mutual coupling (MC) among RIS elements and its impact on localization performance. We tackle the joint estimation of the 3D location of a single-antenna user equipment (UE) and MC coefficients in challenging multipath and LoS-blocked environments. To enhance MC estimation, we extend our analysis to scenarios where signals from multiple UE locations are available, leveraging the stability of MC values over extended time intervals. Our methodology encompasses several key steps: first, we estimate the delay using the multiple signal classification (MUSIC) algorithm to mitigate multipath effects; second, we employ an efficient MC-unaware maximum likelihood (ML) approach for initial 2D angle-of-departure (2D-AOD) estimation; third, we propose a novel closed-form solution for the initial estimation of MC coefficients relying on a scattering matrix-based realistic MC modeling; and finally, we introduce a low-complexity alternating optimization algorithm for the joint refinement of the 2D-AODs and MC values. Simulation results demonstrate the effectiveness of the proposed method, outperforming classical MC-unaware ML techniques.

Index Terms—3D localization, alternating optimization, angle of departure estimation, array imperfection, ISAC, maximum likelihood, mutual coupling, RIS.

I. INTRODUCTION

Realizing the 6G vision for applications such as vehicle-to-everything, smart homes, and smart manufacturing, which require extensive wireless device deployment for sensing and communication, necessitates the integration of communication and sensing within networks. This integration has motivated the recent research focus on integrated sensing and communications (ISAC) [1]–[4]. ISAC has recently gained attention as a powerful approach for delivering dual services and improving spectrum utilization. ISAC is generally achieved by combining communication and sensing in the temporal-spatial domains, with shared frequency bands to enhance efficiency [5], [6].

A. Fadakar is with the Ming Hsieh Department of Electrical and Computer Engineering, University of Southern California, Los Angeles, California, USA; E-mail: fadakarg@usc.edu.

M. F. Keskin, H. Chen and H. Wymeersch are with the Department of Electrical Engineering, Chalmers University of Technology, Sweden, E-mails: {furkan, hui.chen, henkw}@chalmers.se. (*Corresponding author: Hui Chen.*)

This work is supported by the SNS JU project 6G-DISAC under the EU's Horizon Europe research and innovation program under Grant Agreement No 101139130, by the Swedish Research Council (VR) through the project 6G-PERCEF under Grant 2024-04390, and by the Chalmers Area-of-Advance Transport (Project ID 95418010).

These functions complement each other in system design, signal processing, and data analysis, while shared hardware reduces costs. However, resource multiplexing alone cannot fully meet the rising demand for data transmission and device interactions [6]. Furthermore, analyzing the theoretical performance bounds of ISAC systems reveals the interplay between sensing and communication (e.g., competitive or cooperative) in resource utilization, providing insights for efficient physical-layer design [4].

Traditional approaches for improving ISAC performance, such as adding more antennas and spectrum, increase complexity and power consumption [7]. In this regard, reconfigurable intelligent surfaces (RISs) offer a promising solution to overcome ISAC limitations by providing cost-effective, easily deployable, and programmable enhancements [2], [3], [6], [8], [9]. RISs consist of configurable elements (in single- or multi-layer) capable of adjusting signal phases to reshape the wireless channel, which is particularly useful for overcoming line-of-sight (LoS) blockages in mmWave communications [10]–[12]. Recent ISAC methods have often overlooked the potential of position information to improve performance, thereby limiting the spatial resolution benefits provided by RIS arrays [9]. Consequently, achieving *accurate position information is essential for the effective deployment of RIS-aided ISAC systems* in practical wireless channels. Radio positioning can extract information from channel estimations without requiring additional infrastructure [13]–[16]. However, as frequencies increase in 6G systems (e.g., mmWave and sub-THz), signal blockage and attenuation become critical issues [17]. In this context, RISs are expected to play a key role in enhancing both communication and localization performance and coverage [18], [19]. As a result, RISs are expected to further expand the applicability and effectiveness of radio localization in ISAC framework [3], [9], [18].

RIS-assisted localization has been extensively studied in recent years (see, e.g., [9], [16], [18], [20], [21]). In [20], a closed-form least squares (LS) method is proposed for 3D localization using partially connected receiving RISs, which leverages the root multiple signal classification (MUSIC) method for angle estimation. In [21], maximum likelihood (ML) based 2D localization is studied using a single base station (BS) and a single RIS in 2D scenarios. In [16], the absolute 3D positions of user equipments (UEs) are estimated using at least two RISs and sidelink communication between UEs. Additionally, [18] investigates 3D localization and synchronization of a UE with multiple RISs, employing deep learning to enhance 2D-AOD estimation. The authors in

[9], propose a three-step channel reconstruction framework to improve 2D localization and channel estimation using uniform linear array (ULA) equipped RIS and BS. Common to all these works is that hardware impairments at the RIS are ignored, leading to overly optimistic performance predictions. In particular, as RIS technology advances and larger arrays are deployed in ISAC systems, mutual coupling (MC) becomes an increasingly important factor that can greatly influence the performance of RIS-assisted systems [22], [23]. MC arises from the interaction between adjacent RIS elements, where the electromagnetic (EM) fields generated by one element affect the behavior of nearby elements. This interaction can notably degrade the overall performance of various techniques employed in RIS-based deployments, including applications such as localization. Consequently, addressing the impact of MC is vital for enhancing the efficiency and performance of RIS-assisted ISAC systems.

A. Prior MC Work and Motivation

Hardware impairments can significantly impact system performance and complicate hardware design [24]. Such impairments in the antenna array include MC, array gain errors, RIS pixel failures, and antenna displacement errors, among others [19], [25]. Among these impairments, MC distorts the array beampattern and affects angle estimation, which degrades the corresponding position performance [26]. A number of recent studies have contributed to advancements in modeling and optimizing MC effects [23]. In [27], a physics-based end-to-end model is proposed to describe RIS-parametrized wireless channels with adjustable fading characteristics. To capture MC effects in RIS, microwave network theory is often applied. Current approaches to microwave network-based MC modeling in communications are typically classified into *impedance matrix-based models* [28] and *scattering matrix-based models* [23], [29], [30]. In [28], an EM-compliant, MC-aware communication model is introduced by leveraging mutual impedance analysis between RIS elements. In contrast, [29] investigates, for the first time, a scattering matrix-based model using scattering parameter network analysis. Building on this work, [30] proposes a scattering matrix-based MC-aware communication model. It has been shown that the scattering parameter model is more directly related to the radiation pattern and is easier to measure [31].

In terms of signal processing techniques that address hardware impairments, [25] introduces a deep learning-based framework for improved angle of arrival (AOA) estimation in the presence of array imperfections for ULAs. Similarly, [32] proposes an autoencoder for 2D localization across multiple ULA-equipped BSs, accounting for hardware impairments such as MC. However, these supervised learning methods require substantial labeled data for training, making them challenging for practical applications, especially in complex scenarios such as 3D environments and large array systems where labeled data collection is difficult. In [19], the RIS-aided 3D localization is investigated in presence of RIS pixel failures in near-field scenarios. More recently, [23] experimentally investigates the MC effects among RIS elements using an

MC-aware communication model based on scattering matrices. The paper proposes a practical model training approach that leverages a single 3D full-wave simulation of the RIS radiation pattern to estimate the MC parameters. Building on this work, [33] proposes a two-stage approach to address the problems of channel parameter estimation and beamforming in active RIS-assisted communication using sparse recovery techniques. However, these two works assume small values of MC parameters and use linear approximations to relax the problem, which makes them sub-optimal when MC parameters are larger in magnitude.

The RIS-ISAC localization literature [6], [9], [16], [18], [21] generally ignores MC effects. In practice, these methods experience performance degradation due to model mismatch when practical factors, such as MC, cause deviations in the received signals from the assumed mathematical models. As mentioned previously, there have been few recent attempts to address MC in RIS-assisted communication, such as [23] for experimental evaluation of MC in RIS-assisted systems and [33] for channel parameter estimation with an active RIS. However, to the best of our knowledge, this is the first study to address MC in passive RIS-assisted ISAC for localization. In this work, we employ a scattering matrix-based model [23], [30], [34] to characterize MC effects between RIS elements. Specifically, we develop a novel low-complexity algorithm for joint MC parameter estimation and 3D localization of the UE in a challenging multipath environment accounting for both low and severe MC effects.

B. Main Contributions

In this paper, we address the problem of joint localization and RIS MC parameter estimation in RIS-aided ISAC systems. This work represents the first study on RIS-aided joint MC parameter estimation and 3D localization under the impact of MC, relying on a physically realistic scattering-matrix model of MC coefficients. The main contributions are summarized as follows:

- **Generalized RIS-aided localization problem formulation:** We formulate the joint 3D localization and MC scattering parameter estimation problem for a single-antenna UE in a multipath environment, utilizing a uniform planar array (UPA)-equipped RIS and a UPA BS, with LoS blockage in the downlink. The MC values at the RIS are affected by the RIS array structure and the surrounding environment properties such as temperature, and are assumed to remain constant over extended time periods. Leveraging this practical assumption, we extend the problem to include scenarios where the UE records signals from multiple independent locations, improving the accuracy of MC estimation.
- **Novel low-complexity method for initial coarse estimations:** First, the delay between the BS and UE through the RIS is estimated using the MUSIC approach. Then, delay beamforming is applied to mitigate interference and compress the signal, which is subsequently used for joint position and MC parameter estimation. For initial coarse 2D-AOD estimation, we propose an efficient low-complexity MC-unaware ML approach. Additionally, we

derive a closed-form initial estimate of the MC values by relaxing the problem using the first two terms of the Neumann series expansion of the MC-stricken RIS phase profiles.

- **Novel algorithm for joint MC and 3D location estimation refinement:** Next, we introduce an efficient alternating optimization (AO)-based algorithm for the joint refinement of the 2D-AODs and MC values. The estimated delay and 2D-AODs are then employed for UE positioning. In addition, for the first time, we calculate the Cramér-Rao bound (CRB) values for joint localization and MC parameter estimation, providing a benchmark for performance evaluation. Extensive simulations are conducted to validate the superiority of the proposed MC-aware method over traditional ML approach in a challenging multipath environment under MC effects. Furthermore, a comprehensive complexity analysis demonstrates the efficiency of the proposed method.

Notations: Matrices are denoted by bold uppercase letters (e.g., \mathbf{X}) and vectors by bold lowercase letters (e.g., \mathbf{x}). The submatrix $[\mathbf{X}]_{\mathbf{u},\mathbf{v}}$ denotes the rows indexed by \mathbf{u} and columns indexed by \mathbf{v} in \mathbf{X} . Using $:$ in place of \mathbf{u} or \mathbf{v} selects all rows or columns, respectively. The superscripts $(\cdot)^T$, $(\cdot)^H$, and $(\cdot)^{-1}$ represent the transpose, Hermitian, and inverse of a vector or matrix, respectively. The expression $[\mathbf{x}_1, \dots, \mathbf{x}_n]$ denotes the horizontal concatenation of vectors $\mathbf{x}_1, \dots, \mathbf{x}_n$, and $\text{diag}(\mathbf{x})$ indicates a diagonal matrix with the elements of \mathbf{x} on its main diagonal. The notation $\text{diag}(\mathbf{X})$ refers to a vector of the diagonal elements of matrix \mathbf{X} . The $n \times n$ identity matrix is denoted by \mathbf{I}_n , while $\mathbf{I}_{n,i}$ is a matrix whose i -th diagonal elements are ones and zeros elsewhere ($\mathbf{I}_{n,0} = \mathbf{I}_n$). $\mathbf{1}_M$ represents an $M \times 1$ all-ones vector. The norms $\|\mathbf{X}\|_F$ and $\|\mathbf{x}\|$ denote the Frobenius and l_2 norms, respectively. The operations $\mathbf{A} \otimes \mathbf{B}$, $\mathbf{A} \odot \mathbf{B}$, and $\mathbf{A} \oslash \mathbf{B}$ represent the Kronecker product, Hadamard product, and element-wise division, respectively. Finally, $\mathbb{S}[\mathbf{X}]$ denotes the sum of all elements in \mathbf{X} .

II. SYSTEM MODEL

As illustrated in Fig. 1a, the considered ISAC system includes a multi-antenna BS, a single passive RIS, and a single-antenna UE, which performs localization after receiving N_u downlink pilot observations from the BS at different positions. We assume the BS and RIS are equipped with a UPA, comprising M_b and M_r elements, respectively. Let M_1 and M_2 be the number of rows and columns of the RIS, respectively. Moreover, $\mathbf{p}_b \in \mathbb{R}^3$, $\mathbf{p}_r \in \mathbb{R}^3$, and $\mathbf{p}_u \in \mathbb{R}^3$ present the position of the centers of the BS, the RIS, and the UE, respectively. We assume that the LoS path between the BS and UE is blocked. Additionally, we assume that the RIS location and orientation are known at both the BS and UE, while the BS position and orientation are also known at the UE. Moreover, we assume that time and frequency synchronization are achieved via a round-trip time (RTT) protocol by exploiting known preamble signals [35], allowing us to focus on AOD estimation and UE positioning. Additionally, scatter points (SPs) are used to model the non-line-of-sight

(NLoS) paths for the multipath effect, which will be detailed in subsequent sections.

A. Signal Model

The BS communicates with the UE through the RIS by transmitting orthogonal frequency division multiplexing (OFDM) pilots over N_s subcarriers across N_t transmissions. The subcarrier spacing, denoted by Δf , can be determined by $\Delta f = W/N_s$, where W represents the bandwidth. After stacking all $N_s N_t$ received signals over all N_t transmissions and N_s subcarriers, we obtain the matrix $\mathbf{Y} \in \mathbb{C}^{N_s \times N_t}$ at the UE as

$$\mathbf{Y} = \mathbf{Y}_B + \mathbf{Y}_R + \mathbf{N}, \quad (1)$$

where $\mathbf{N} \in \mathbb{C}^{N_s \times N_t}$ denotes the additive white Gaussian noise matrix where $[\mathbf{N}]_{i,j} \sim \mathcal{CN}(0, \sigma_n^2)$ and $\sigma_n^2 = WN_0$ with N_0 denoting the noise spectral density (PSD). Moreover, $\mathbf{Y}_R \in \mathbb{C}^{N_s \times N_t}$ represents the received downlink signal matrix over the RIS-reflected path, and $\mathbf{Y}_B \in \mathbb{C}^{N_s \times N_t}$ denotes the received signal component resulting from uncontrolled (i.e., scatterer-induced NLoS) paths between the BS and the UE. To represent the multipath effect, we adopt the geometric channel model [16], [18]. Thus, the matrices in (1) can be defined as:

$$\mathbf{Y}_B = \mathbf{H}_{\text{BSU}} \odot \mathbf{X} \quad (2)$$

$$= \sum_{i=1}^{N_{\text{BSU}}} \alpha_{\text{bsu}}^{(i)} \mathbf{d}(\tau_{\text{bsu}}^{(i)}) \mathbf{q}_{\text{bsu}}^{(i)T} \odot \mathbf{X}$$

$$\mathbf{Y}_R = (\mathbf{H}_{\text{BRU}} + \mathbf{H}_{\text{BSRU}} + \mathbf{H}_{\text{BRSU}}) \odot \mathbf{X} \quad (3)$$

$$= \alpha_{\text{bru}} [\mathbf{d}(\tau_{\text{bru}}) (\mathbf{b}_{\text{bru}} \odot \mathbf{q}_{\text{bru}})^T] \odot \mathbf{X}$$

$$+ \sum_{i=1}^{N_{\text{BSRU}}} \alpha_{\text{bsru}}^{(i)} [\mathbf{d}(\tau_{\text{bsru}}^{(i)}) (\mathbf{b}_{\text{bsru}}^{(i)} \odot \mathbf{q}_{\text{bsru}}^{(i)})^T] \odot \mathbf{X}$$

$$+ \sum_{i=1}^{N_{\text{BRSU}}} \alpha_{\text{brsu}}^{(i)} [\mathbf{d}(\tau_{\text{brsu}}^{(i)}) (\mathbf{b}_{\text{brsu}}^{(i)} \odot \mathbf{q}_{\text{brsu}}^{(i)})^T] \odot \mathbf{X}.$$

Here, \mathbf{H}_{BSU} , \mathbf{H}_{BRU} , \mathbf{H}_{BSRU} , and \mathbf{H}_{BRSU} denote the BS-SP-UE, BS-RIS-UE, BS-SP-RIS-UE, and BS-RIS-SP-UE channel matrices, respectively with corresponding complex channel gains $\alpha_{\text{bsu}}^{(i)}$, α_{bru} , $\alpha_{\text{bsru}}^{(i)}$, and $\alpha_{\text{brsu}}^{(i)}$. N_{BSU} , N_{BSRU} , and N_{BRSU} are the number of paths in the corresponding NLoS channels. The pilot matrix $\mathbf{X} \in \mathbb{C}^{N_s \times N_t}$ is defined as $\mathbf{X} = \sqrt{P} \mathbf{X}'$, where P denotes the BS transmitted power, and \mathbf{X}' represents the transmitted unit modulus complex valued symbols across N_s subcarriers and N_t transmissions.

In the following, the components used in (2) and (3) are mathematically detailed and explained.

1) *Delay Steering Vector and Delays of Paths:* Delay steering vector $\mathbf{d}(\cdot) \in \mathbb{C}^{N_s}$ is defined

$$\mathbf{d}(\tau) = [1, e^{-j\xi_1 \tau}, \dots, e^{-j\xi_{N_s-1} \tau}]^T, \quad (4)$$

where $\xi_n = 2\pi n \Delta f$. Since we assume that the UE and the BS are synchronized, the delays $\tau_{\text{bsu}}^{(i)}$, τ_{bru} , $\tau_{\text{bsru}}^{(i)}$, and $\tau_{\text{brsu}}^{(i)}$ are defined as

$$\tau_{\text{bsu}}^{(i)} = \frac{\|\mathbf{p}_u - \mathbf{p}_{\text{bsu}}^{(i)}\| + \|\mathbf{p}_{\text{bsu}}^{(i)} - \mathbf{p}_b\|}{c}, \quad (5)$$

$$\tau_{\text{bru}} = \frac{\|\mathbf{p}_u - \mathbf{p}_r\| + \|\mathbf{p}_r - \mathbf{p}_b\|}{c},$$

$$\tau_{\text{bsru}}^{(i)} = \frac{\|\mathbf{p}_u - \mathbf{p}_r\| + \|\mathbf{p}_r - \mathbf{p}_{\text{bsru}}^{(i)}\| + \|\mathbf{p}_{\text{bsru}}^{(i)} - \mathbf{p}_b\|}{c},$$

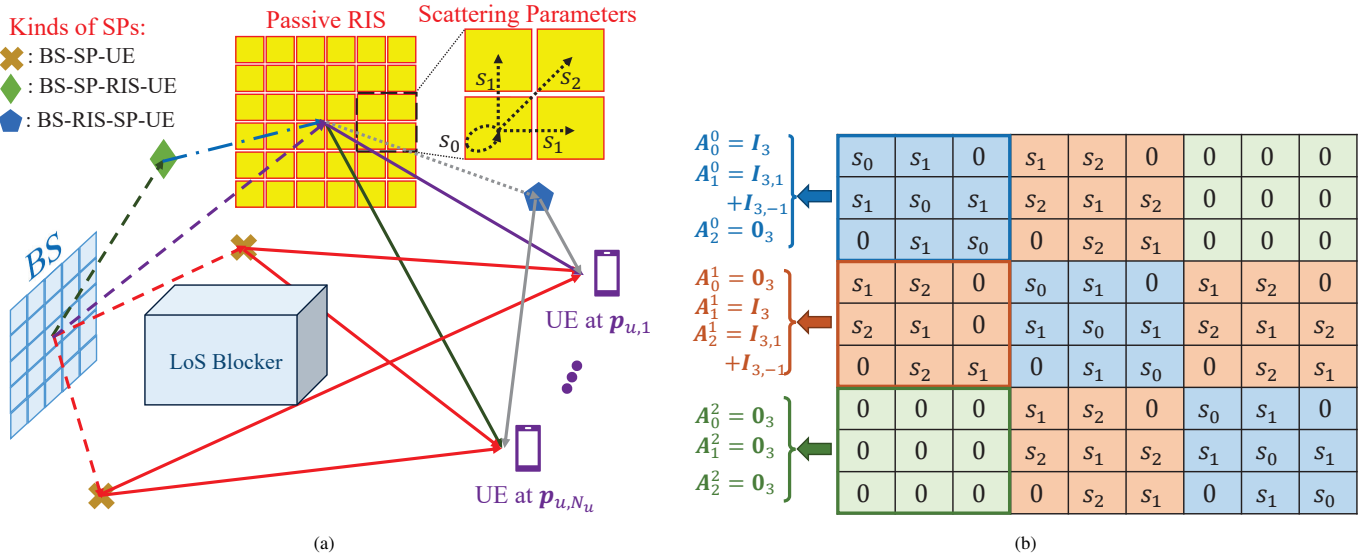


Fig. 1: (a) Considered RIS assisted ISAC System. This paper aims to jointly estimate UE positions and scattering parameters. (b) Scattering matrix \mathbf{S} for $M_1 = M_2 = 3$ and $B_m = 2$.

$$\tau_{\text{brsu}}^{(i)} = \frac{\|\mathbf{p}_u - \mathbf{p}_{\text{brsu}}^{(i)}\| + \|\mathbf{p}_{\text{brsu}}^{(i)} - \mathbf{p}_r\| + \|\mathbf{p}_r - \mathbf{p}_b\|}{c},$$

where $\mathbf{p}_{\text{bsu}}^{(i)}$, $\mathbf{p}_{\text{brsu}}^{(i)}$, and $\mathbf{p}_{\text{brsu}}^{(i)}$ denote the position of the i -th SP in the BS-SP-UE, BS-SP-RIS-UE, and BS-RIS-SP-UE channels, respectively.

2) *Modeling the Impact of RIS Phase Modulation:* The vectors \mathbf{b}_{bru} , $\mathbf{b}_{\text{brsu}}^{(i)}$, and $\mathbf{b}_{\text{brsu}}^{(i)}$ account for the effect of the RIS's phase modulation whose t -th elements can be obtained as

$$\begin{aligned} [\mathbf{b}_{\text{bru}}]_t &= \mathbf{a}_r^T(\psi_{r,u}^d) \Omega'_t \mathbf{a}_r(\psi_{b,r}^a), \\ [\mathbf{b}_{\text{brsu}}^{(i)}]_t &= \mathbf{a}_r^T(\psi_{r,u}^d) \Omega'_t \mathbf{a}_r(\psi_{\text{sru}}^{a(i)}), \\ [\mathbf{b}_{\text{brsu}}^{(i)}]_t &= \mathbf{a}_r^T(\psi_{\text{rsu}}^{d(i)}) \Omega'_t \mathbf{a}_r(\psi_{b,r}^a). \end{aligned} \quad (6)$$

where $\Omega'_t \in \mathbb{C}^{M_r \times M_r}$ represents the unknown MC affected phase control coefficients of the RIS during the t -th transmission [30, Eq. (5)], [34, Eq. (8)] [23, Eq. (7)]:

$$\Omega'_t = (\Omega_t^{-1} - \mathbf{S})^{-1}, \quad (7)$$

where $\Omega_t \in \mathbb{C}^{M_r \times M_r}$ denotes the RIS phase profile in the t -th transmission, and $\mathbf{S} \in \mathbb{C}^{M_r \times M_r}$ represents the scattering matrix for modeling MC whose details are provided in Section II-B. It is important to emphasize that the matrices Ω_t are *designer-controlled* and thus known in advance. However, since the scattering matrix \mathbf{S} is *unknown* a priori, the MC affected RIS phase profiles Ω'_t are also *unknown*. In (6), the RIS steering vector $\mathbf{a}_r(\cdot) \in \mathbb{C}^{M_r}$ is defined as

$$\mathbf{a}_r(\boldsymbol{\psi}) = e^{jk\mathbf{D}_r^T \mathbf{u}(\boldsymbol{\psi})}, \quad (8)$$

where $\mathbf{D}_r \in \mathbb{R}^{3 \times M_r}$ is a matrix whose i -th column indicates the coordinates of the i -th element of the RIS, and $\mathbf{u}(\boldsymbol{\psi})$ denotes the unit direction from the RIS corresponding to either 2D-AOA or 2D-AOD $\boldsymbol{\psi} = [\theta, \phi]^T$ which can be obtained as $\mathbf{u}(\boldsymbol{\psi}) = [\cos(\theta) \cos(\phi), \cos(\theta) \sin(\phi), \sin(\theta)]^T$.

In (6), $\psi_{b,r}^a = [\theta_{b,r}^a, \phi_{b,r}^a]^T$ denotes the 2D-AOA from the BS to the RIS. $\theta_{b,r}^a$ and $\phi_{b,r}^a$ are the elevation (angle between \mathbf{u} and XY-plane) and azimuth (angle between the projection of \mathbf{u} on the XY-plane and the X-axis) AOAs, respectively, which

can be obtained as follows:

$$\theta_{b,r}^a = \arccos\left(\frac{[\mathbf{p}_{b;r}]_3}{\|\mathbf{p}_{b;r}\|}\right), \quad \phi_{b,r}^a = \arctan2([\mathbf{p}_{b;r}]_2, [\mathbf{p}_{b;r}]_1), \quad (9)$$

where $\mathbf{p}_{b;r} = \mathbf{R}_r^T(\mathbf{p}_b - \mathbf{p}_r)$, with $\mathbf{R}_r \in \mathbb{R}^{3 \times 3}$ being the rotation matrix corresponding to the orientation of the RIS. The 2D-AODs and 2D-AOAs $\psi_{r,u}^d$, $\psi_{\text{bsu}}^{d(i)}$, $\psi_{\text{bsu}}^{a(i)}$, $\psi_{\text{sru}}^{d(i)}$, $\psi_{\text{sru}}^{a(i)}$ and $\psi_{\text{rsu}}^{d(i)}$ are defined similarly, where the superscripts d and a indicate the AODs and AOAs, respectively, and subscripts b , r , u , and s represent the BS, RIS, UE, and SP, respectively.

3) *Modeling the Impact of BS Phase Modulation:* The vectors \mathbf{q}_{bru} and $\mathbf{q}_{\text{brsu}}^{(i)}$ in (3), and the vector $\mathbf{q}_{\text{bsu}}^{(i)}$ in (2) represent the gain of the BS beamforming towards RIS, the i -th BS-SP-RIS-UE path and the i -th BS-SP-UE path, respectively, which can be written as

$$\mathbf{q}_{\text{bru}} = \mathbf{a}_b^T(\psi_{b,r}^d) \mathbf{F}, \quad \mathbf{q}_{\text{brsu}}^{(i)} = \mathbf{a}_b^T(\psi_{\text{sru}}^{d(i)}) \mathbf{F}, \quad \mathbf{q}_{\text{bsu}}^{(i)} = \mathbf{a}_b^T(\psi_{\text{bsu}}^{d(i)}) \mathbf{F}, \quad (10)$$

where $\mathbf{F} \in \mathbb{C}^{M_b \times N_t}$ denotes the BS beamforming matrix over N_t transmissions, where $\mathbf{a}_b(\cdot) \in \mathbb{C}^{M_b}$ is the BS steering vector which is defined similar to (8).

B. Modeling Scattering Matrix for Mutual Coupling

In (7), $\mathbf{S} \in \mathbb{C}^{M_r \times M_r}$ represents the scattering matrix of the RIS antenna network. To model MC, we adopt the realistic model proposed in [23], [33], which has been validated through real measurements in [23]. In the following, we present and formulate this model for a general UPA-equipped RIS and represent it using banded symmetric matrices.

1) *Number of Unique Scattering Values:* Define the parameter B_m to determine the number of elements each element of the RIS can influence depending on its row or column index difference. The number of unique scattering values, denoted by N_m , corresponds to the number of unique distances each RIS element can influence, based on B_m . Thus, N_m can be uniquely determined from B_m . For instance, if $B_m = 2$, the total of $N_m = 3$ scattering values exists. Fig. 1a and Fig. 1b

illustrate the significance of these values which are shown with $\{s_i\}_{i=0}^2$.

2) *Representation of the Scattering Matrix Using Banded Symmetric Matrices:* Let $\mathbf{A}_i \in \mathbb{Z}^{M_r \times M_r}$ denote the support matrix of the S-parameter $s_i \in \mathbb{C}$. In particular, $[\mathbf{A}_i]_{k,l} = 1$ if the voltage wave s_i is measured at the k -th element of the RIS when a unit voltage wave is applied at the l -th element of the RIS. For instance for s_0 , $\mathbf{A}_0 = \mathbf{I}_{M_r}$. The matrix \mathbf{A}_i for $i > 0$ can be obtained using symmetric banded Toeplitz block matrices.

In the rest of the paper, it is assumed that the indices of the RIS elements are counted horizontally, starting from the first row and first column. Based on this assumption, define $\mathbf{A}_i^{u,v} \in \mathbb{C}^{M_2 \times M_2}$ to denote the (u, v) -th block matrix in \mathbf{A}_i , which represents the effects of the u -th row¹ of the RIS on the elements of the v -th row by the scattering parameter s_i . Assuming all elements of the RIS are identical and experience the same physical conditions, such as temperature, we deduce that for any pair (u, v) with a fixed absolute difference $w = |u - v|$, the blocks $\mathbf{A}_i^{u,v}$ are identical. For simplicity, we define $\mathbf{A}_i^w = \mathbf{A}_i^{u,v}$. Thus, \mathbf{A}_i^w captures how rows with an absolute index difference w influence each other through the scattering parameter s_i . Once the matrices \mathbf{A}_i^w are defined, the scattering matrix \mathbf{S} is uniquely determined. For instance, for $B_m = 2$, as shown in Fig. 1b, the nonzero block matrices can be expressed as:

$$\begin{aligned} i = 0 : \mathbf{A}_0^0 &= \mathbf{I}_{M_2}, \\ i = 1 : \mathbf{A}_1^0 &= \mathbf{I}_{M_2,1} + \mathbf{I}_{M_2,-1}, \quad \mathbf{A}_1^1 = \mathbf{I}_{M_2}, \\ i = 2 : \mathbf{A}_2^1 &= \mathbf{I}_{M_2,1} + \mathbf{I}_{M_2,-1}. \end{aligned} \quad (11)$$

It is important to note that in general there is no closed-form expression to model these block matrices, as their definitions depend on the value of B_m . However, in practical scenarios, each RIS element has a stronger influence on its nearby elements, leading to $s_i > s_j$ for $i < j$. Therefore, the effects of MC between sufficiently distant RIS elements can be neglected for simplicity [23]. Hence, we can assume that B_m is sufficiently small and fixed. Finally, the scattering matrix \mathbf{S} can be modeled as [23, Eq. (15)]:

$$\mathbf{S} \approx \sum_{i=0}^{N_m-1} s_i \mathbf{A}_i. \quad (12)$$

We emphasize that while the support matrices $\{\mathbf{A}_i\}_{i=1}^{N_m-1}$ and B_m (and thus N_m) are known a priori, the matrix \mathbf{S} remains unknown due to the unknown MC parameters $\{s_i\}_{i=0}^{N_m-1}$.

Remark 1. *This study focuses on developing mathematical and algorithmic solutions to jointly estimate the UE positions and MC scattering values $\{s_i\}_{i=0}^{N_m-1}$, independent of their specific structure or values. Thus, the proposed methodologies remain applicable irrespective of environmental variations such as temperature and humidity. To demonstrate this, Section VI evaluates our approach under diverse scenarios and varying MC conditions.*

¹Notably, if RIS elements are counted vertically instead of horizontally, the matrices $\mathbf{A}_i^{u,v}$ will represent the MC effects between the u -th and v -th columns (with dimensions $M_1 \times M_1$) rather than rows; however, both cases yield equivalent results.

C. Beamforming and RIS Phase Profile Design

In this subsection, we explain the proposed beamforming approach for designing BS precoders and RIS phase profiles. First, we derive the directional codebook for the considered uncertainty region, and then we explain the proposed method.

1) *Directional Codebook for BS precoders:* Since the locations of the BS and RIS \mathbf{p}_b and \mathbf{p}_r are known beforehand, the angles $\psi_{b,r}^a, \psi_{b,r}^d$ are also known. Thus, we design the BS precoders using the optimal directional beamforming vector in all N_t transmissions to concentrate the power P towards the RIS, which maximizes the SNR at the RIS [18], [21], [36]. Hence, the directional BS beamforming matrix \mathbf{F} (defined in Section II-A3) is designed as

$$\mathbf{F} = \mathbf{a}_b^* (\psi_{b,r}^d) \mathbf{1}_{N_t}^T. \quad (13)$$

2) *Directional Codebook for RIS Phase Profiles:* Let \mathcal{U} denote the 3D uncertainty volume in which the UE resides, and moreover, let \mathcal{U}^ψ be the corresponding 2D uncertainty region in 2D-AOD (θ - ϕ) plane. Define $\Theta = [\theta_{\min}, \theta_{\max}]$ and $\Phi = [\phi_{\min}, \phi_{\max}]$ as the smallest intervals for elevation and azimuth AODs in \mathcal{U}^ψ , respectively. The intervals are then uniformly divided with grid steps d_θ and d_ϕ , respectively, resulting in a uniform $N_\theta \times N_\phi$ mesh grid of 2D-AODs, which is used to construct the directional codebook. However, since \mathcal{U}^ψ is not necessarily rectangle, those 2D-AODs whose Euclidean distance from \mathcal{U}^ψ are less than a threshold ϵ_b are removed, resulting in $N_t \leq N_\theta N_\phi$ 2D-AODs $\mathcal{U}_D^\psi \in \mathbb{R}^{2 \times N_t}$, where the subscript \mathcal{D} accounts for the directional codebook. Let $\mathbf{W}_D \in \mathbb{C}^{M_r \times N_t}$ represent all directional beams towards these N_t 2D-AODs. Using (8), the t -th directional beam is defined as:

$$[\mathbf{W}_D]_{:,t} = \mathbf{a}_r^*([\mathcal{U}_D^\psi]_{:,t}) \odot \mathbf{a}_r^*(\psi_{b,r}^a), \quad (14)$$

where the second term $\mathbf{a}_r^*(\psi_{b,r}^a)$ is multiplied to remove the effect of the known 2D-AOA from the BS to the RIS. For the t -th transmission, the MC-unaware directional RIS phase coefficients are given by $\Omega_t = \text{diag}([\mathbf{W}_D]_{:,t})$.

3) *Adaptive Codebook for RIS Phase Profiles:* Existing channel estimation and localization methods require substantial pilot overhead to probe multiple reflected channels. While advanced extensions aim to reduce this, their dependence on the number of reflecting elements limits their practicality in RIS deployments [37]. In particular, although the directional codebook in (14) is widely used in the literature [18], [21], it has a significant drawback: as the RIS size increases, the resulting beams become narrower and more focused [38]. Consequently, a larger RIS requires more directional beams to adequately cover the angular uncertainty region, which in turn leads to an increased number of beams, higher complexity, and greater channel overhead.

To mitigate this issue, inspired by [38], we first divide \mathcal{U}^ψ into N_t non-overlapping rectangles with widths d_θ and d_ϕ with the centers $\mathcal{U}_A^\psi \in \mathbb{R}^{2 \times N_t}$ covering the entire \mathcal{U}^ψ . Next, each rectangle is uniformly divided into $M_1 \times M_2$ rectangular grids with widths $\frac{d_\theta}{M_1} \times \frac{d_\phi}{M_2}$. Then, for the adaptive codebook $\mathbf{W}_A \in \mathbb{C}^{M_r \times N_t}$ the phase of the (m_1, m_2) -th element of the RIS in the t -th transmission is steered towards the (m_1, m_2) -th

grid as:

$$[\mathbf{W}_{\mathcal{A}}]_{I(m_1, m_2), t} = e^{-jk\mathbf{D}_{:, I(m_1, m_2)}^T \mathbf{u}(\boldsymbol{\psi}_{I(m_1, m_2)}^t)} \times [\mathbf{a}_r^*(\boldsymbol{\psi}_{b, r}^a)]_{I(m_1, m_2)} \quad (15)$$

where $I(m_1, m_2) = M_2(m_1 - 1) + m_2$ is the 1D index of the element in the m_1 -th row and m_2 -th column of the RIS (the indices are counted horizontally starting with the element on the first row and first column), and $\boldsymbol{\psi}_{I(m_1, m_2)}^t \in \mathbb{R}^2$ denotes the 2D-AOD with respect to the center of the (m_1, m_2) -th rectangular grid in the t -th rectangle which can be obtained as:

$$[\boldsymbol{\psi}_{I(m_1, m_2)}^t]_1 = [\mathbf{U}_{\mathcal{A}}^\psi]_{1, t} + \left(\frac{2m_1 - M_1 - 1}{2M_1} \right) d_\theta, \quad (16)$$

$$[\boldsymbol{\psi}_{I(m_1, m_2)}^t]_2 = [\mathbf{U}_{\mathcal{A}}^\psi]_{2, t} + \left(\frac{2m_2 - M_2 - 1}{2M_2} \right) d_\phi.$$

Remark 2. The choice of grid sizes d_θ and d_ϕ , which determine N_t , involves a trade-off. Larger grids produce wider beams, reducing N_t and channel overhead but lowering the SNR, thereby increasing theoretical lower bounds. Conversely, smaller grids yield more directive beams and higher SNR, tightening lower bounds and improving localization accuracy at the cost of increased N_t and higher channel overhead.

III. DELAY ESTIMATION AND SIGNAL COMPRESSION

Fig. 2 presents the block diagram of the proposed methodology, which is executed at the UE upon receiving the downlink signals from the BS during the return leg of the RTT protocol. The figure illustrates the interconnections between the various processing modules and their respective functionalities. This section focuses on the signal compression module, while the subsequent section elaborates on the remaining components of the proposed framework.

First, we employ the widely adopted MUSIC approach for delay estimation. Next, the estimated delays are utilized to reduce the signal dimension and compress the data, which is then employed for joint 2D-AOD and MC parameter estimation in subsequent sections.

A. MUSIC Method for Delay Estimation

By assuming that the transmitted symbol matrix \mathbf{X}' is known at the UE, we first remove its impact via reciprocal filtering $\tilde{\mathbf{Y}} = \mathbf{Y} \circledast \mathbf{X}' = \tilde{\mathbf{Y}}_B + \tilde{\mathbf{Y}}_R + \tilde{\mathbf{N}}$, where $\tilde{\mathbf{Y}}_B = \mathbf{Y}_B \circledast \mathbf{X}'$, $\tilde{\mathbf{Y}}_R = \mathbf{Y}_R \circledast \mathbf{X}'$, and $\tilde{\mathbf{N}} = \mathbf{N} \circledast \mathbf{X}'$. Next, we compute the frequency-domain sample covariance matrix (SCM) [39], [40] of the matrix $\tilde{\mathbf{Y}}$ defined as

$$\mathbf{R}_y = \frac{1}{N_t} \tilde{\mathbf{Y}} \tilde{\mathbf{Y}}^H = E_{\text{bru}} \mathbf{d}(\tau_{\text{bru}}) \mathbf{d}^H(\tau_{\text{bru}}) + \sum_{i=1}^{N_{\text{BSU}}} E_{\text{bsu}}^{(i)} \mathbf{d}(\tau_{\text{bsu}}^{(i)}) \mathbf{d}^H(\tau_{\text{bsu}}^{(i)}) + \sum_{i=1}^{N_{\text{BSRU}}} E_{\text{bsru}}^{(i)} \mathbf{d}(\tau_{\text{bsru}}^{(i)}) \mathbf{d}^H(\tau_{\text{bsru}}^{(i)}) + \sum_{i=1}^{N_{\text{BRSU}}} E_{\text{brsu}}^{(i)} \mathbf{d}(\tau_{\text{brsu}}^{(i)}) \mathbf{d}^H(\tau_{\text{brsu}}^{(i)}) + \mathbf{R}_n, \quad (17)$$

where $\mathbf{R}_n = \tilde{\mathbf{N}} \tilde{\mathbf{N}}^H / N_t$ denotes the SCM of the noise matrix. It is important to note that in (17), the cross terms are neglected under the assumption that the number of subcarriers N_s is

sufficiently large, ensuring that the delays of different paths do not overlap. A similar analysis to that in [41] can be applied for the proof. Additionally:

$$E_{\text{bru}} = P |\alpha_{\text{bru}}|^2 (\mathbf{b}_{\text{bru}} \odot \mathbf{q}_{\text{bru}})^T (\mathbf{b}_{\text{bru}} \odot \mathbf{q}_{\text{bru}})^*, \quad (18)$$

$$E_{\text{bsu}}^{(i)} = P |\alpha_{\text{bsu}}^{(i)}|^2 \mathbf{q}_{\text{bsu}}^{(i)T} \mathbf{q}_{\text{bsu}}^{(i)*},$$

$$E_{\text{bsru}}^{(i)} = P |\alpha_{\text{bsru}}^{(i)}|^2 (\mathbf{b}_{\text{bsru}}^{(i)} \odot \mathbf{q}_{\text{bsru}}^{(i)})^T (\mathbf{b}_{\text{bsru}}^{(i)} \odot \mathbf{q}_{\text{bsru}}^{(i)})^*,$$

$$E_{\text{brsu}}^{(i)} = P |\alpha_{\text{brsu}}^{(i)}|^2 (\mathbf{b}_{\text{brsu}}^{(i)} \odot \mathbf{q}_{\text{brsu}}^{(i)})^T (\mathbf{b}_{\text{brsu}}^{(i)} \odot \mathbf{q}_{\text{brsu}}^{(i)})^*$$

denote the total power in the corresponding paths in each subcarrier. Next, to reduce the coherence effect in multipath scenario in (17), we adopt forward backward spatial smoothing (FBSS) scheme which makes the paths more separable by reducing the coherence between the paths [42], [43]. The smoothed SCM by the FBSS algorithm is calculated as

$$\mathbf{R}_{fy} = \frac{1}{2} (\mathbf{R}_y + \mathbf{J} \mathbf{R}_y^* \mathbf{J}), \quad (19)$$

where $\mathbf{J} \in \mathbb{Z}^{N_s \times N_s}$ indicates an exchange matrix with ones on its antidiagonal and zeros elsewhere. Next, we perform eigen value decomposition (EVD) as

$$\mathbf{R}_{fy} = \mathbf{U} \text{diag}(\boldsymbol{\lambda}) \mathbf{U}^H = \sum_{n=1}^{N_s} \lambda_n \mathbf{u}_n \mathbf{u}_n^H, \quad (20)$$

where the vector $\boldsymbol{\lambda} = [\lambda_1, \dots, \lambda_{N_s}]^T$ contains the eigen values of \mathbf{R}_{fy} in an increasing order i.e., $\lambda_1 \geq \dots, \lambda_{N_s}$. In this paper, we are only interested in using the BS-RIS-UE path signal for joint positioning and MC estimation. In fact, the channel measurements have shown that the power of the RIS-reflected path component is higher than the sum of the power of NLoS paths [36], [44]. However, to be able to accurately estimate the number of paths in the BS-UE channel, we employ the minimum description length (MDL) [45] algorithm. Thus, let \hat{N} be the estimated number of paths by MDL. Then, we define the noise subspace $\mathbf{U}_N = [\mathbf{U}]_{:, \hat{N}+1: N_s}$. Finally, we obtain the MUSIC spectrum $\mathbf{s}_M \in \mathbb{R}^{N_\tau}$, whose i -th element can be obtained as follows:

$$[\mathbf{s}_M]_i = \frac{1}{\mathbf{d}^H(\tau_i) \mathbf{U}_N \mathbf{U}_N^H \mathbf{d}(\tau_i)}, \quad (21)$$

where $\tau_i \in [\tau_{\min}, \tau_{\max}]$ is the i -th delay on the grid. Here, τ_{\min} and τ_{\max} are the minimum and maximum possible delays of the BS-RIS-UE path each UE may exhibit inside the uncertainty area \mathcal{U} , respectively. Thus, the RIS-reflected path delay τ_{bru} is estimated by finding the largest peak of the MUSIC spectra, which is denoted as $\hat{\tau}_{\text{bru}}$.

B. Compressed Observation Signals

To suppress the impact of NLoS paths and ensure that the compressed observation primarily captures the contribution of the LoS path, we perform signal compression by applying delay beamforming. To this end, the vector $\mathbf{d}^*(\hat{\tau}_{\text{bru}})$ is multiplied by $\tilde{\mathbf{Y}}^T$ to obtain the compressed vector $\hat{\mathbf{y}} \in \mathbb{C}^{N_t}$ as follows:

$$\hat{\mathbf{y}} = \tilde{\mathbf{Y}}^T \mathbf{d}^*(\hat{\tau}_{\text{bru}}) = \gamma_{\text{bru}} \mathbf{b}_{\text{bru}} + \sum_{i=1}^{N_{\text{BSU}}} \gamma_{\text{bsu}}^{(i)} \mathbf{1}_{N_t} + \sum_{i=1}^{N_{\text{BSRU}}} \gamma_{\text{bsru}}^{(i)} \mathbf{b}_{\text{bsru}}^{(i)} + \sum_{i=1}^{N_{\text{BRSU}}} \gamma_{\text{brsu}}^{(i)} \mathbf{b}_{\text{brsu}}^{(i)} + \tilde{\mathbf{n}}. \quad (22)$$

Here, we used the fact that all of the BS beams are identical (see (13)) which leads to the simplified BS phase modu-

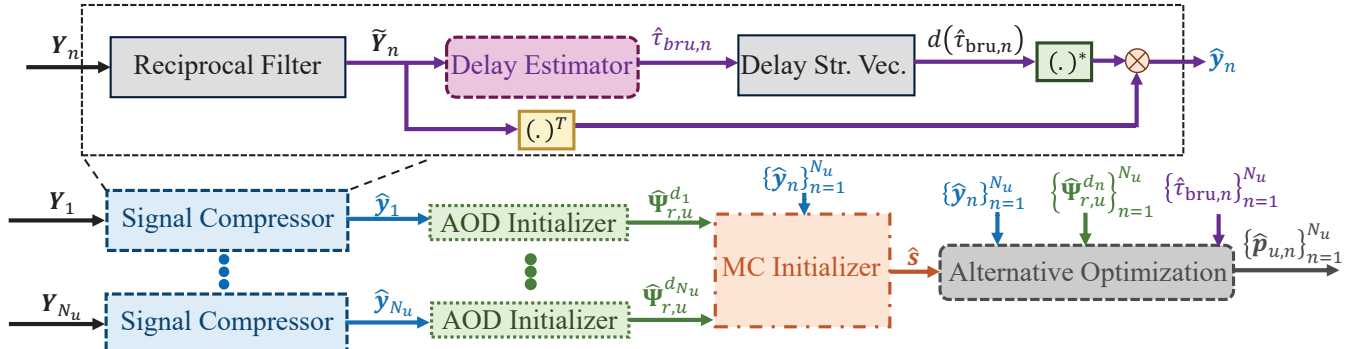


Fig. 2: Block diagram for the overall proposed scheme and the connections between different processing modules.

lation vectors (defined in (10)): $\mathbf{q}_{bru} = u_{bru} \mathbf{1}_{N_t}$, $\mathbf{q}_{bsru}^{(i)} = u_{bsru}^{(i)} \mathbf{1}_{N_t}$, $\mathbf{q}_{bsu}^{(i)} = u_{bsu}^{(i)} \mathbf{1}_{N_t}$, where

$$u_{bru} = \mathbf{a}_b^T(\boldsymbol{\psi}_{b,r}^d) \mathbf{a}_b^*(\boldsymbol{\psi}_{b,r}^d) = M_b,$$

$$u_{bsru}^{(i)} = \mathbf{a}_b^T(\boldsymbol{\psi}_{sru}^{d(i)}) \mathbf{a}_b^*(\boldsymbol{\psi}_{b,r}^d),$$

$$u_{bsu}^{(i)} = \mathbf{a}_b^T(\boldsymbol{\psi}_{bsu}^{d(i)}) \mathbf{a}_b^*(\boldsymbol{\psi}_{b,r}^d),$$

denote the gains of the BS beamforming towards each path. Moreover, $\tilde{\mathbf{n}} = \tilde{\mathbf{N}}^T \mathbf{d}^*(\hat{\tau}_{bru})$ is the resulted noise. The total gains γ_{bru} , $\gamma_{bsu}^{(i)}$, $\gamma_{bsru}^{(i)}$, and $\gamma_{bsu}^{(i)}$ are obtained as follows:

$$\gamma_{bru} = \alpha_{bru} u_{bru} g_{bru}, \quad \gamma_{bsu}^{(i)} = \alpha_{bsu}^{(i)} u_{bsu}^{(i)} g_{bsu}^{(i)}, \quad (23)$$

$$\gamma_{bsru}^{(i)} = u_{bsru}^{(i)} \alpha_{bsru}^{(i)} g_{bsru}^{(i)}, \quad \gamma_{bsu}^{(i)} = \alpha_{bsu}^{(i)} u_{bsu}^{(i)} g_{bsu}^{(i)}$$

where $g_{bru} = \mathbf{d}(\tau_{bru})^T \mathbf{d}(\hat{\tau}_{bru})^* \approx N_s$, $g_{bsu}^{(i)} = \mathbf{d}(\tau_{bsu}^{(i)})^T \mathbf{d}(\hat{\tau}_{bru})^*$, $g_{bsru}^{(i)} = \mathbf{d}(\tau_{bsru}^{(i)})^T \mathbf{d}(\hat{\tau}_{bru})^*$, $g_{bsu}^{(i)} = \mathbf{d}(\tau_{bsu}^{(i)})^T \mathbf{d}(\hat{\tau}_{bru})^*$, denote the gains of delay beamforming. Notably, higher bandwidth (i.e., an increased number of subcarriers assuming a fixed frequency spacing) improves delay resolution, thereby enhancing multi-path filtering for delays $\tau \neq \tau_{bru}$.

IV. JOINT LOCALIZATION AND MC COEFFICIENT ESTIMATION

A. Optimization Problem Formulation

It is important to note that the MC values depend on the antenna's own excitation, physical structure, the environmental characteristics such as humidity and temperature, and contributions from adjacent antenna elements. Thus, by using the same BS beamforming and RIS phase profiles, as explained in Section II-C, over multiple consecutive blocks of transmissions, the MC values remain constant during these time intervals. Motivated by this observation, we extend the problem to improve the precision of MC coefficient estimation by considering multiple blocks of transmissions. Specifically, we assume N_u blocks, each consisting of N_t transmissions. These blocks do not necessarily occur consecutively. Let $\mathbf{p}_{u,n}$ denote the position of the UE in the n -th block. For simplicity, we assume that the state of the UE is independent across blocks and that the channel remains quasi-static within each block. Given the compressed observation signals $\{\hat{\mathbf{y}}_n\}_{n=1}^{N_u}$ (obtained in (22)), the generalized problem is stated as follows:

$$\underset{\mathbf{s}, \{\boldsymbol{\psi}_{r,u}^{d_n}\}_{n=1}^{N_u}}{\text{minimize}} \quad \sum_{n=1}^{N_u} \|\hat{\mathbf{y}}_n - \gamma_n \mathbf{b}_n\|^2 \quad (24a)$$

$$\text{s.t.} \quad [\mathbf{b}_n]_t = \mathbf{a}_r^T(\boldsymbol{\psi}_{r,u}^{d_n}) \boldsymbol{\Omega}'_t \mathbf{a}_r(\boldsymbol{\psi}_{b,r}^a), \quad (24b)$$

$$t \in \mathcal{T}_n, n = 1, \dots, N_u, \quad (24c)$$

$$\boldsymbol{\Omega}'_t = (\boldsymbol{\Omega}_t^{-1} - \mathbf{S})^{-1}, \quad (24c)$$

$$\mathbf{S} = \sum_{i=0}^{N_m-1} s_i \mathbf{A}_i, \quad (24d)$$

where $\mathcal{T}_n \in \mathbb{R}^{N_t}$ denotes the index of transmissions made when the UE is located at $\mathbf{p}_{u,n}$, and the subscript n is used for variables or parameters associated with $\mathbf{p}_{u,n}$. Moreover, $\mathbf{s} = [s_0, s_1, \dots, s_{N_m-1}]^T$ denotes the vector of MC coefficients. Following this, the optimal values of the complex gain coefficients $\{\gamma_n\}_{n=1}^{N_u}$ are derived using the ML criterion as follows:

$$\gamma_n = \mathbf{b}_n^H \hat{\mathbf{y}}_n / \|\mathbf{b}_n\|^2, \quad n = 1, \dots, N_u. \quad (25)$$

Substituting (25) back to the objective function (24a) we have:

$$\sum_{n=1}^{N_u} \|\hat{\mathbf{y}}_n - \gamma_n \mathbf{b}_n\|^2 = \sum_{n=1}^{N_u} \left[\|\hat{\mathbf{y}}_n\|^2 - |\mathbf{b}_n^H \hat{\mathbf{y}}_n|^2 / \|\mathbf{b}_n\|^2 \right]. \quad (26)$$

Since $\|\hat{\mathbf{y}}_n\|^2$ does not depend on the optimization variables, using (26) the optimization problem (24) can be simplified as:

$$\underset{\mathbf{s}, \{\boldsymbol{\psi}_{r,u}^{d_n}\}_{n=1}^{N_u}}{\text{maximize}} \quad \sum_{n=1}^{N_u} |\mathbf{b}_n^H \hat{\mathbf{y}}_n|^2 / \|\mathbf{b}_n\|^2 \quad (27a)$$

$$\text{s.t.} \quad (24b), (24c), (24d)$$

The objective (27a) is non-convex, and the constraint (24c) makes the problem more challenging. To make the problem more tractable, inspired by the real MC measurements presented in [23], we assume that the magnitudes of the MC values are sufficiently small in this paper. This assumption implies that the scattering matrix \mathbf{S} in (24c) can be considered a perturbation of the inverse MC-unaware RIS phase profile $\boldsymbol{\Omega}_t^{-1}$. As will be shown in Section VI-C, if $\|\mathbf{s}\| < 0.5$, the spectral radius of the matrix $\boldsymbol{\Omega}_t \mathbf{S}$ is less than one. Thus, the constraint (24c) can be represented by employing the Neumann series expansion as follows [23, Eq. (18)]:

$$\boldsymbol{\Omega}'_t = (\boldsymbol{\Omega}_t^{-1} - \mathbf{S})^{-1} = \sum_{n=0}^{\infty} (\boldsymbol{\Omega}_t \mathbf{S})^n \boldsymbol{\Omega}_t \approx \sum_{n=0}^{N_w} (\boldsymbol{\Omega}_t \mathbf{S})^n \boldsymbol{\Omega}_t, \quad (28)$$

where all notations were initially defined in (7). The infinite Neumann series is approximated by retaining only terms with powers up to N_w , leveraging the fact that $\max |s_i|^{(N_w+1)}$

becomes sufficiently small². To address the problem in (27), we first substitute (28) into (24b). Then, assuming that the initial estimates of $\{\psi_{r,u}^{d_n}\}_{n=1}^{N_u}$ and \mathbf{s} are available, we propose an alternating refinement approach that jointly optimizes the estimated 2D-AODs and MC values. The details are provided in the following subsections.

B. Initial 2D-AOD Estimation

To obtain an initial estimation of 2D-AODs in an efficient manner, we relax the constraint (24b) by assuming an MC free scenario i.e., $\mathbf{s} = \mathbf{0}_{N_m}$. With this assumption, the RIS phase configuration vector \mathbf{b} for the 2D-AOD ψ can be rewritten as:

$$\mathbf{b}^T(\psi) = (\mathbf{a}_r(\psi) \odot \mathbf{a}_r(\psi_{b,r}^a))^T \mathbf{W}, \quad (29)$$

where $\mathbf{W} \in \{\mathbf{W}_D, \mathbf{W}_A\}$ denotes the chosen RIS phase profile codebook. For initial AOD estimation, \mathbf{U}^ψ is divided into grids with elevation and azimuth steps, c_θ and c_ϕ , respectively, resulting in a set of 2D-AODs $\psi_c \in \mathbb{R}^{2 \times N_c}$. Then, for each grid point $[\psi_c]_{:,i}$, we compute (29) and normalize the result to obtain the vector $\mathbf{b}([\psi_c]_{:,i}) / \|\mathbf{b}([\psi_c]_{:,i})\|$. By stacking the obtained vectors, the matrix $\mathbf{B} \in \mathbb{C}^{N_t \times N_c}$ is formed. The grid point yielding the maximum objective value (27a) is selected as the initial estimate of the 2D-AOD. Thus, the 2D-AOD of the n -th location can be estimated as:

$$\hat{\psi}_{r,u}^{d_n} = [\psi_c]_{:, \arg \max_i |[\mathbf{B}^H \hat{\mathbf{y}}_n]_i|}. \quad (30)$$

It is noteworthy that to improve efficiency, the matrix \mathbf{B} can be computed once and reused for initial 2D-AOD estimation at any location.

C. Initial MC Coefficient Estimation

1) *RIS Profile Matrix Approximation*: Although in (28) we approximated the MC-affected RIS profile using the first $N_w + 1$ terms of the Neumann series, our simulations indicate that the first order also provides a consistent, albeit less accurate, estimation. Thus, for the sole purpose of obtaining an initial estimation of the MC coefficients, we only keep the first two terms and approximate Ω'_t as:

$$\Omega'_t \approx \Omega_t + \Omega_t \mathbf{S} \Omega_t = \Omega_t + \sum_{i=0}^{N_m-1} s_i \Omega_t \mathbf{A}_i \Omega_t. \quad (31)$$

Hence, the zero-order and first-order estimations of the vector \mathbf{b} , denoted by $\mathbf{b}^{(0)}$ and $\mathbf{b}^{(1)}$ respectively, can be obtained as:

$$[\mathbf{b}_n^{(0)}]_t = \mathbf{a}_r^T(\hat{\psi}_{r,u}^{d_n}) \Omega_t \mathbf{a}_r(\psi_{b,r}^a), \quad (32)$$

$$[\mathbf{b}_n^{(1)}]_t = [\mathbf{b}_n^{(0)}]_t + \sum_{i=0}^{N_m-1} s_i \mathbf{a}_r^T(\hat{\psi}_{r,u}^{d_n}) \Omega_t \mathbf{A}_i \Omega_t \mathbf{a}_r(\psi_{b,r}^a).$$

2) *MC Vector Linear Estimation*: After stacking all N_t terms in (32) at the location $\mathbf{p}_{u,n}$:

$$\mathbf{b}_n^{(1)} = \mathbf{b}_n^{(0)} + \mathbf{L}_n \mathbf{s}, \quad (33)$$

where $\mathbf{L}_n \in \mathbb{C}^{N_t \times N_m}$ is a matrix whose (t, i) -th element is defined as:

$$[\mathbf{L}_n]_{t,i} = \mathbf{a}_r^T(\hat{\psi}_{r,u}^{d_n}) \Omega_t \mathbf{A}_i \Omega_t \mathbf{a}_r(\psi_{b,r}^a). \quad (34)$$

Thus, the n -th term in the objective function (24a) is relaxed as follows:

$$\|\hat{\mathbf{y}}_n - \hat{\gamma}_n \mathbf{b}_n^{(1)}\| = \|\hat{\mathbf{y}}_n - \hat{\gamma}_n (\mathbf{b}_n^{(0)} + \mathbf{L}_n \mathbf{s})\|, \quad (35)$$

²Although we approximate the RIS phase profile in (28) for the sake of algorithm development, we will employ the exact definition in the CRB calculation and generating data in simulations section to evaluate the performance of the proposed algorithms.

where $\hat{\gamma}_n$ denotes the estimated value for γ_n obtained by substituting $\mathbf{b}_n^{(0)}$ in (25). Hence, using LS technique, the vector $\mathbf{L}_n \mathbf{s}$ can be estimated as:

$$\mathbf{L}_n \mathbf{s} \approx \frac{1}{\hat{\gamma}_n} (\hat{\mathbf{y}}_n - \hat{\gamma}_n \mathbf{b}_n^{(0)}). \quad (36)$$

Thus, after stacking the equation (36) for $n = 1, \dots, N_u$, a closed form estimation of MC vector \mathbf{s} using the LS technique can be obtained as:

$$\hat{\mathbf{s}} = \mathbf{L}_{\text{tot}}^\dagger (\bar{\mathbf{y}}_{\text{tot}} - \mathbf{b}_{\text{tot}}^{(0)}), \quad (37)$$

where $\mathbf{L}_{\text{tot}} \in \mathbb{C}^{N_t N_u \times N_m}$ is a matrix obtained by stacking the matrices in the set $\{\mathbf{L}_n\}_{n=1}^{N_u}$, and similarly the vectors $\bar{\mathbf{y}}_{\text{tot}} \in \mathbb{C}^{N_t N_u}$, and $\mathbf{b}_{\text{tot}}^{(0)}$ are the defined by stacking the vectors in the sets $\{\hat{\mathbf{y}}_n / \hat{\gamma}_n\}_{n=1}^{N_u}$ and $\{\mathbf{b}_n^{(0)}\}_{n=1}^{N_u}$, respectively.

D. Proposed Algorithm for Joint Localization and MC Coefficients Estimation

Finally, we propose an AO-based algorithm to jointly refine the 2D-AODs and MC values. Specifically, at each step, we first fix the MC values and, for each location, update the corresponding 2D-AODs $\hat{\psi}_{r,u}^{d_n}$ by finding the ML estimate that maximize the n -th component in (27) using the fast derivative-free Nelder-Mead (NM) algorithm. Next, we fix the 2D-AODs $\{\hat{\psi}_{r,u}^{d_n}\}_{n=1}^{N_u}$ and update the MC vector $\hat{\mathbf{s}}$ via gradient descent (GD) based approach. This procedure is repeated until convergence, which occurs when the maximum change in optimization variables, i.e., the 2D-AODs or the MC vector, is less than a predefined threshold, or when the maximum number of iterations exceeds N_{itt}^{\max} . The average number of iterations is reported in Section V-C3. After the algorithm converges, the 3D position of the UE at the location $\mathbf{p}_{u,n}$ can be estimated as

$$\tilde{\mathbf{p}}_{u,n} = c \hat{\tau}_{\text{bru},n} \hat{\mathbf{u}}_n, \quad \hat{\mathbf{p}}_{u,n} = \mathbf{R}_r \tilde{\mathbf{p}}_{u,n} + \mathbf{p}_r, \quad (38)$$

where $\hat{\mathbf{u}}_n$ is the unit direction towards the estimated 2D-AOD $\hat{\psi}_{r,u}^{d_n}$, and $\tilde{\mathbf{p}}_{u,n}$ denotes the estimated position in the local coordinates of the RIS, and finally $\hat{\mathbf{p}}_{u,n}$ is the estimated UE position in the global coordinates.

The overall proposed algorithm for joint positioning and MC coefficients estimation is detailed in Algorithm 1.

In each iteration of the NM and GD algorithms in lines 8 and 9, the objective function (or its derivative) (27) needs to be evaluated. Thus, for efficient optimization, we need to calculate the vectors \mathbf{b}_n (defined in (24b)) in a low-complexity manner. The dominant part contributing to the complexity, is the calculation of MC affected RIS phase profiles (28). Considering the fact that the support matrices \mathbf{A}_i are fixed, we first expand the $(l+1)$ -th term (order l) in the Neumann series as follows:

$$(\Omega_t \mathbf{S})^l \Omega_t = \left(\sum_{i=0}^{N_m-1} s_i \Omega_t \mathbf{A}_i \right)^l \Omega_t = \sum_{j=1}^{N_m^l} s_j^{(l)} \mathbf{A}_j^{(l,t)}, \quad (39)$$

where

$$s_j^{(l)} = \prod_{i=1}^l s_{[\mathbf{c}_l]_{j,i}}, \quad \mathbf{A}_j^{(l,t)} = \prod_{i=1}^l \Omega_t \mathbf{A}_{[\mathbf{c}_l]_{j,i}}, \quad (40)$$

where $\mathbf{c}_l \in \mathbb{Z}^{N_m^l \times l}$ is a matrix whose rows represent all permutations of length l from the set $\{0, \dots, N_m - 1\}$. Moreover, as discussed before, the steering vector $\mathbf{a}_r(\psi_{b,r}^a)$ is constant and can be considered fixed during optimization. Thus, for each $l = 1, \dots, N_w$, we define the 3D array $\mathbf{Q}_l \in \mathbb{C}^{N_t \times M_r \times N_m^l}$ to

store all vectors used during optimization which is defined as follows:

$$[\mathbf{Q}_l]_{t,:j} = \begin{cases} \boldsymbol{\Omega}_t \mathbf{a}_r(\psi_{b,r}^a) & l = 0, j = 1 \\ \mathbf{A}_j^{(l,t)} \mathbf{a}_r(\psi_{b,r}^a) & 1 \leq l \leq N_w, 1 \leq j \leq N_m^l, \end{cases} \quad (41)$$

Thus, for given 2D-AOD ψ and MC vector \mathbf{s} , the vector \mathbf{b}_n in (24b), can be calculated as:

$$[\mathbf{b}_n]_t = \sum_{l=1}^{N_w} \mathbb{S}[(\mathbf{a}_r^T(\psi)[\mathbf{Q}_l]_{t,:}) \odot \mathbf{s}_l^T], \quad (42)$$

where $\mathbf{s}_l \in \mathbb{C}^{N_m^l}$ is defined according to (40) as $[\mathbf{s}_l]_j = s_j^{(l)}$. It is easy to see that we can obtain and rewrite \mathbf{s}_l in more simplified form as follows:

$$\mathbf{s}_l = \begin{cases} 1 & l = 0 \\ \underbrace{\mathbf{s} \otimes \dots \otimes \mathbf{s}}_{l \text{ times}} = \mathbf{s}^{\otimes l} & 1 \leq l \leq N_w. \end{cases} \quad (43)$$

In Section V-C3, the lower complexity of (42) is demonstrated compared to the direct calculation using (28) through obtaining complexities using big-O notation.

Algorithm 1 Proposed Joint Positioning and MC Estimation Algorithm

- 1: **Inputs:** Signals $\{\mathbf{Y}_n\}_{n=1}^{N_u}$ at N_u positions $\{\mathbf{p}_{u,n}\}_{n=1}^{N_u}$.
 - 2: **Output:** Estimated 3D positions $\{\hat{\mathbf{p}}_{u,n}\}_{n=1}^{N_u}$ and MC coefficients $\hat{\mathbf{s}}$.
 - 3: For $n = 1, \dots, N_u$, perform MUSIC method according to Section III on \mathbf{Y}_n to estimate $\hat{\tau}_{\text{bru},n}$ and obtain compressed observation signal $\hat{\mathbf{y}}_n$ using (22).
 - 4: Find initial estimates $\{\hat{\psi}_{r,u}^{d_n}\}_{n=1}^{N_u}$ of 2D-AODs using (30).
 - 5: Find an initial estimation $\hat{\mathbf{s}}$ of MC values based on the closed-form solution based on (37).
 - 6: **repeat**
 - 7: **for** $n = 1, \dots, N_u$ **do**
 - 8: Update the 2D-AOD $\hat{\psi}_{r,u}^{d_n}$ by maximizing the n -th component in (27) using the Nelder-Mead algorithm, keeping the other variables fixed.
 - 9: **end for**
 - 10: Update the estimated MC vector $\hat{\mathbf{s}}$ by maximizing (27) using gradient descent approach. Keep other variables fixed during the optimization.
 - 11: **until convergence**
 - 12: Obtain the estimated positions $\{\hat{\mathbf{p}}_{u,n}\}_{n=1}^{N_u}$ using (38).
-

We provide a convergence analysis of the algorithm in the following proposition.

Proposition 1. *If the initial estimated values for the 2D-AODs in (30) and the MC vector in (37) are sufficiently accurate, then Algorithm 1 converges to the optimal solution of the optimization problem (27).*

Proof. Please see Appendix A.

V. LOWER BOUND AND COMPLEXITY ANALYSIS

In this section, first we perform a Fisher information analysis to obtain the CRBs for the channel and state parameters

for performance analysis. Then, we perform an extensive complexity analysis for each part of the proposed approach.

A. CRB in the Channel Domain

It is important to emphasize that the CRB analysis in this subsection is based on the signal model containing only the RIS-reflected BS-RIS-UE path in (3), rather than the general signal model in (1). Thus, the model used for CRB calculation differs from the generative model in (1) used to generate observations in the simulations. As a result, the CRB calculation considers a simplified, mismatched model, which may yield optimistic bounds in the presence of interference. For the optimization problem in (24), we compute the Fisher information matrix (FIM) of the unknown channel parameter vector $\boldsymbol{\rho} \in \mathbb{R}^{5N_u+2N_m}$, which is defined as follows:

$$[\boldsymbol{\rho}]_{5(n-1)+1:5n} = [\psi_{r,u}^{d_n}, \tau_{\text{bru},n}, \rho_{\text{bru},n}, \varphi_{\text{bru},n}]^T, \quad 1 \leq n \leq N_u, \quad (44)$$

$[\boldsymbol{\rho}]_{5N_u+2i-1} = \Re\{[\mathbf{s}]_i\}$, $[\boldsymbol{\rho}]_{5N_u+2i} = \Im\{[\mathbf{s}]_i\}$, $1 \leq i \leq N_m$, where we have split the real and imaginary parts of the MC parameters. Since the observations in (1) are complex Gaussian, the FIM $\mathcal{I}_{\boldsymbol{\rho}} \in \mathbb{R}^{(5N_u+2N_m) \times (5N_u+2N_m)}$ can be obtained using the Slepian-Bangs formula [21]. In particular, the (i, j) -th element of $\mathcal{I}_{\boldsymbol{\rho}}$ can be calculated as:

$$[\mathcal{I}_{\boldsymbol{\rho}}]_{i,j} = \sum_{n=1}^{N_u} \mathbb{S} \left[\Re \left\{ \left(\frac{\partial \mathbf{Y}_n^f}{\partial [\boldsymbol{\rho}]_i} \right)^* \odot \left(\frac{\partial \mathbf{Y}_n^f}{\partial [\boldsymbol{\rho}]_j} \right) \right\} \right], \quad (45)$$

where \mathbf{Y}_n^f denotes the multipath and noise free observation matrix at the position $\mathbf{p}_{u,n}$. Thus, we can define the delay and 2D-AOD error bounds (EBs) as follows:

$$\text{EB}_{\theta_n} = \sqrt{[\mathcal{I}_{\boldsymbol{\rho}}^{-1}]_{5(n-1)+1,5(n-1)+1}}, \quad (46)$$

$$\text{EB}_{\phi_n} = \sqrt{[\mathcal{I}_{\boldsymbol{\rho}}^{-1}]_{5(n-1)+2,5(n-1)+2}},$$

$$\text{EB}_{\tau_n} = \sqrt{[\mathcal{I}_{\boldsymbol{\rho}}^{-1}]_{5(n-1)+3,5(n-1)+3}}. \quad (47)$$

Hence, the 2D-AOD EB at the location $\mathbf{p}_{u,n}$ is defined as $\text{EB}_{\psi_n} = \sqrt{\text{EB}_{\theta_n}^2 + \text{EB}_{\phi_n}^2}$. Finally, the total delay and 2D-AOD EBs accounting for all the observations at N_u locations, are defined as the root mean squared (RMS) of the individual EBs:

$$\text{EB}_{\psi} = \sqrt{\frac{1}{N_u} \sum_{n=1}^{N_u} \text{EB}_{\psi_n}^2}, \quad \text{EB}_{\tau} = \sqrt{\frac{1}{N_u} \sum_{n=1}^{N_u} \text{EB}_{\tau_n}^2}. \quad (48)$$

B. CRB for 3D Localization and MC Estimation

The vector of location and MC parameters $\boldsymbol{\eta} \in \mathbb{R}^{5N_u+2N_m}$ is defined as follows

$$[\boldsymbol{\eta}]_{5(n-1)+1:5n} = [\mathbf{p}_{u,n}, \rho_{\text{bru},n}, \varphi_{\text{bru},n}]^T, \quad 1 \leq n \leq N_u, \quad (49)$$

$$[\boldsymbol{\eta}]_{5N_u+2i-1} = \Re\{[\mathbf{s}]_i\}, \quad [\boldsymbol{\eta}]_{5N_u+2i} = \Im\{[\mathbf{s}]_i\}, \quad 1 \leq i \leq N_m.$$

It is noteworthy that the channel gains $\{\rho_{\text{bru},n}, \varphi_{\text{bru},n}\}_{n=1}^{N_u}$ and the MC vector \mathbf{s} are nuisance parameters, as they do not provide any geometric information relevant for localization. Consequently, these parameters cannot be expressed as functions of other unknown geometric variables. As such, they appear in both the channel and location domain parameter vectors in (44) and (49).

To derive the FIM in the location domain, we perform a variable transformation from the channel vector $\boldsymbol{\rho}$ to the

state vector η . Thus, the FIM of η , denoted as \mathcal{I}_η , is obtained using the Jacobian transformation matrix $\mathbf{T} = \frac{\partial \mathbf{g}^T}{\partial \eta} \in \mathbb{R}^{(5N_u+2N_m) \times (5N_u+2N_m)}$ as $\mathcal{I}_\eta = \mathbf{T} \mathcal{I}_g \mathbf{T}^T$. Thus, the position EB (PEB) at $\mathbf{p}_{u,n}$ is obtained as:

$$\text{PEB}_n = \sqrt{\text{tr}([\mathcal{I}_\eta^{-1}]_{5(n-1)+1:5(n-1)+3:5(n-1)+1:5(n-1)+3})}. \quad (50)$$

Similar to (48), we define the total average PEB by applying RMS on the corresponding PEBs at all N_u positions as

$$\text{PEB} = \sqrt{\frac{1}{N_u} \sum_{n=1}^{N_u} \text{PEB}_n^2}. \quad (51)$$

Finally, the EB for the MC vector can be calculated as:

$$\text{EB}_{\text{MC}} = \sqrt{\text{tr}([\mathcal{I}_\eta^{-1}]_{5N_u+1:5N_u+2N_m, 5N_u+1:5N_u+2N_m})}. \quad (52)$$

C. Complexity Analysis

1) *Complexity of Delay Estimation:* The computation of the SCM in (17) requires a complexity of $O(N_s^2 N_t)$. Additionally, the EVD in (20) incurs a complexity of $O(N_s^3)$ [14], and the MUSIC spectrum in (21) is obtained with a complexity of $O(N_\tau N_s^2)$, where N_τ denotes the number of delay grids. Hence, the overall complexity of the delay estimation is given by:

$$\mathcal{O}_1 = O(N_s^2 N_t) + O(N_s^3) + O(N_\tau N_s^2). \quad (53)$$

2) *Complexities of Initial 2D-AOD and MC Estimation:*

The proposed MC-unaware ML method for 2D-AOD estimation in (30) has a computational complexity of $\mathcal{O}_2 = O(N_c N_t)$. For the proposed closed-form initial MC estimation in (37), the dominant computational cost stems from computing the pseudo-inverse of the matrix \mathbf{L}_{tot} , which, assuming $N_m \leq N_t N_u$, requires a complexity of $\mathcal{O}_3 = O(N_t N_u N_m^2)$.

3) *Complexity of the Proposed Refinement Algorithm:* The complexity of computing the vector \mathbf{b}_n using (42) is given by:

$$O(N_t M_r (1 + \sum_{l=0}^{N_w} N_m^l)) = O(N_t N_m^{N_w+1} M_r) \quad (54)$$

It is important to note that as explained before, the MC effect diminishes as the distance between two elements increases, resulting in N_m typically being small (less than 5). Furthermore, as will be demonstrated in the simulation results, setting $N_w = 4$ yields sufficiently accurate MC estimation. Consequently, the term $N_m^{N_w+1}$ in (54) remains small. The total complexity of the proposed Algorithm 1 can be expressed as:

$$\mathcal{O}_4 = O(N_{\text{it}}(N_{\text{nm}} N_u + N_{\text{gd}}) N_t N_m^{N_w+1} M_r) \quad (55)$$

where N_{it} denotes the average number of iterations of the proposed Algorithm 1 until convergence. Moreover, N_{nm} and N_{gd} indicate the average number of the iterations of the NM and GD algorithms in lines 8 and 9 of the algorithm, respectively. According to our simulations, the average number of iterations are $N_{\text{it}} = 7.3$, $N_{\text{nm}} = 17.3$, and $N_{\text{gd}} = 8.2$. Finally, the total complexity of the proposed method can be obtained as $\mathcal{O} = \sum_{i=1}^4 \mathcal{O}_i$ ³.

³It is noteworthy that in real-time scenarios, by assuming MC values vary smoothly over time, previously estimated MC measurements and UE positions can serve as initialization points, accelerating convergence and reducing the required iterations N_{it} , N_{nm} , and N_{gd} . A detailed real-time complexity analysis is left for future research.

If the direct relation in (28) was used to compute Ω'_t , the total computational complexity of the algorithm would be

$$O(N_{\text{it}}(N_{\text{nm}} N_u + N_{\text{gd}}) N_t (N_m M_r^2 + N_w^2 M_r^3)), \quad (56)$$

which shows that as M_r dominates the computational complexity due to its larger value, the proposed computation approach in (42) is approximately M_r^2 times faster than using the direct definition (28), demonstrating its efficiency.

Remark 3. *The complexity of the proposed method scales linearly with M_r . Moreover, since all equations and techniques are derived for a general UPA-shaped RIS, the methodology is independent of specific RIS sizes. As a result, the approach remains scalable to larger RISs with only linear complexity growth, provided the UE position lies in the far-field of the RIS.*

VI. SIMULATION RESULTS

In this section, we evaluate the performance of the proposed joint 3D localization and MC coefficients estimation for RIS-assisted ISAC mmWave systems through numerical simulations.

A. Simulation Setup

The scenario under consideration includes a BS, an RIS, and a single UE, which can record signals at multiple independent locations. The default system parameters are presented in Table I. In all simulations we use maximum of $N_u = 9$ UE locations $\{\mathbf{p}_{u,n}\}_{n=1}^{N_u}$, as shown in Fig. 3b. Note that some parameters may vary in different simulations. Moreover, we set the number of SPs to $N_{\text{BSU}} = 2$, $N_{\text{BSRU}} = 2$, and $N_{\text{BRSU}} = 2$ whose positions are depicted in Fig. 3b. In all simulations, we assume $B_m = 2$, resulting in $N_m = 3$ MC coefficients. The default unit norm MC vector \mathbf{s} is shown in Table I⁴. For simulations where $\|\mathbf{s}\| = \beta$, we scale the default \mathbf{s} from Table I by β to achieve the desired norm. For generating data, for each of the considered UE positions (which is a subset of the UE positions shown in Fig. 3b), using (1) we generate the received signals resulting in matrices $\{\mathbf{Y}_n\}_{n=1}^{N_u}$. According to the selected uncertainty region \mathcal{U} in Table I, the elevation and azimuth range AODs defined in Section II-C are $[\theta_{\min}, \theta_{\max}] = [-11.3^\circ, 11.3^\circ]$ and $[\phi_{\min}, \phi_{\max}] = [-45^\circ, 45^\circ]$, respectively. These intervals are uniformly sampled with a grid step of $d_\theta = d_\phi = \frac{1.8}{15}$ rad $\approx 6.875^\circ$, resulting in $N_t = 59$ 2D-AODs \mathcal{U}_D^ψ as shown in Fig. 3a.

B. Evaluation of RIS Profiles

In this subsection, we compare the performance of directional and adaptive RIS codebooks by computing the PEB values within the plane $-10 < x < 30$ and $2 < y < 40$, with a fixed height of $z = 2$. The results are presented in Fig. 4. Fig. 4a and Fig. 4b show the PEB values for $M_1 = M_2 = 20$ using directional and adaptive codebooks, respectively, while Fig. 4c and Fig. 4d depict the results for a larger RIS with $M_1 = M_2 = 40$. In both scenarios, the number of transmissions is fixed at $N_t = 59$, and the centers \mathcal{U}_A^ψ of

⁴The MC values used in this paper are derived from a realistic scattering matrix-based model proposed in [23], [33], exhibiting a similar level of magnitude. This model has been validated through real measurements in [23].

⁵These values are set according to the half power beamwidth of the RIS with the shape 15×15 .

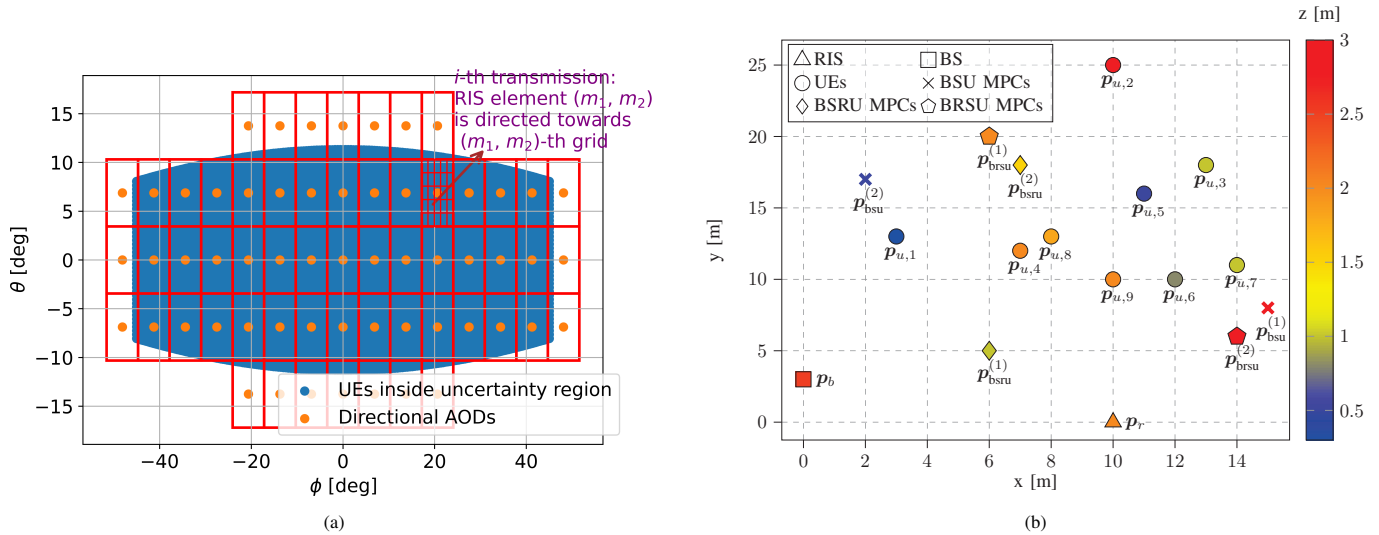


Fig. 3: (a) All possible 2D-AODs of the UE within the uncertainty region \mathcal{U} are shown as blue circles. The UE is moved in 0.1 m increments, and the corresponding 2D-AODs from the RIS are calculated. Directional codebook AODs are indicated by orange circles. For adaptive beamforming, rectangles with dimensions (d_θ, d_ϕ) are formed around each 2D-AOD, subdivided into $M_1 \times M_2$ grids, and RIS elements are directed towards the corresponding grids as (16). (b) BS, RIS, UE, and SP in simulation environment. The colorbar shows the z coordinate values.

TABLE I: System parameters

Default System Parameters	Symbol	Value
Carrier frequency	f_c	30 GHz
Noise PSD	N_0	-173.855 dBm
Light speed	c	3×10^8
Subcarrier bandwidth	Δf	240 kHz
Number of subcarriers	N_s	50
MC vector	s	$[0.606 + 0.308j, -0.234 + 0.614j, 0.0375 - 0.324j]^T$
Uncertainty region	\mathcal{U}	$0 < x < 20, 10 < y < 30, 0 < z < 4$
Number of UE locations	N_u	$1 \leq N_u \leq 9$
BS position	p_b	$[0, 3, 2.5]^T$ [m]
BS number of elements	M_b	$20 \times 20 = 400$
RIS position	p_r	$[10, 0, 2]^T$ [m]
RIS number of elements	M_r	$20 \times 20 = 400$

rectangles in the adaptive codebook are considered the same as the 2D-AODs \mathcal{U}_D^ψ . As shown in Fig. 4c, and as discussed in Section II-C, the directional codebook struggles to generalize for larger RISs, failing to cover all points in the uncertainty region and requiring a higher number of beams. In contrast, the adaptive codebook can more homogeneously cover the entire uncertainty region with the same number of beams.

C. Approximated RIS Phase Profile Evaluation

In this subsection, we assess the validity and accuracy of the Neumann series approximation used in (28) for modeling the RIS phase profile under MC effects. To achieve this, for a given value of $\|s\|$, we randomly generate a scattering matrix \mathbf{S} and diagonal matrix $\mathbf{\Omega}$, where the diagonal elements of $\mathbf{\Omega}$ are unit modulus with random phases uniformly distributed between $-\pi$ and π . We then compute the spectral radius of the matrix $\mathbf{\Omega}\mathbf{S}$ (i.e., the largest eigenvalue in magnitude). This process is repeated 1000 times, and the average spectral radius $\mathbb{E}\{\lambda_{\max}(\mathbf{\Omega}\mathbf{S})\}$ is plotted against $\|s\|$ in Fig. 5a. As shown, the spectral radius approaches one when $\|s\| = 0.5$, indicating that the approximation in (28) holds only when $\|s\| < 0.5$.

A similar simulation is conducted to evaluate the accuracy of the Neumann expansion in (28) for different values of N_w . The relative Frobenius norm error is used as the performance metric, which is plotted against $\|s\|$ in Fig. 5b. As shown, larger values of N_w lead to more precise estimates;

however, the rate of accuracy improvement diminishes as $\|s\|$ approaches 0.5. For the subsequent simulations, we set $N_w = 4$, as this value provides sufficient accuracy for joint localization and MC parameter estimation.

D. Channel Parameters, Position, and MC Estimation Results

In this subsection, we evaluate the performance of the proposed method by analyzing the root mean squared error (RMSE) of the proposed algorithm at different power levels. The CRB values are used as a benchmark for comparison. A total of $N_u = 3$ fixed UE locations is considered, corresponding to the first three positions $\{p_{u,n}\}_{n=1}^3$ shown in Fig. 3b. The proposed method in Algorithm 1 is applied for joint MC and location estimation in a multipath (MP)-free environment. For each $\|s\| \in \{0, 0.2\}$ and power level $P \in \{10, 15, 20, 25, 30\}$ dBm, a total of $N_{\text{gen}} = 500$ data samples are generated for each position, resulting in $N_{\text{gen}}N_u = 1500$ data samples for a given power and $\|s\|$. To evaluate the effect of MP interference, we also consider the case where $\|s\| = 0.2$ in the presence of all SPs shown in Fig. 3b, accounting for MP.

1) *Delay Estimation Performance:* The delay estimation RMSE is illustrated in Fig. 6a. As expected, since the delay estimation process relies solely on the energy of the beamformed signals, defined in (18) (i.e., E_{bru} for the main path), the results remain unaffected by MC. The slight improvement in RMSE can be attributed to small power variations in E_{bru} , caused by different RIS phase profiles corresponding to various values of $\|s\|$.

In a MP scenario, to show how the different paths manifest in the delay domain, the MUSIC spectra have been plotted for three power levels $P \in \{15, 30, 60\}$ dBm using the signal at location $p_{u,1}$ in Fig. 6b. The number of detected paths by the MDL algorithm are 2, 3, and 4, respectively. It can be observed that, at higher power levels, more paths can be detected and distinguished, leading to improved estimation accuracy. Moreover, it is noteworthy that the delays corresponding to

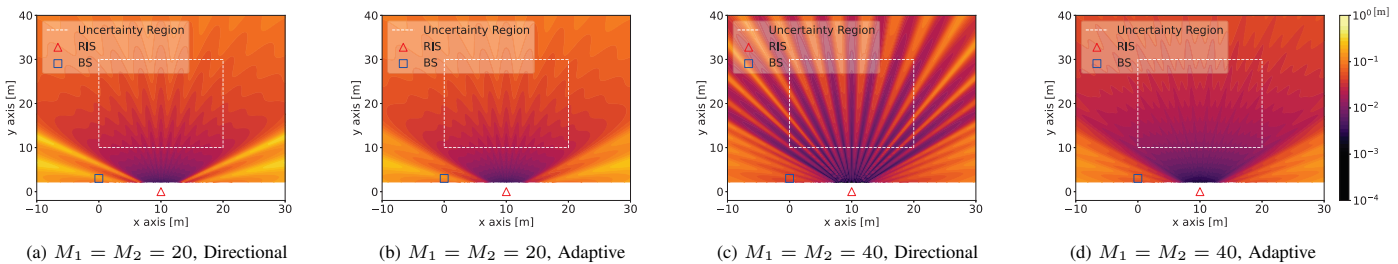


Fig. 4: Comparison of directional and adaptive RIS codebooks by calculating the PEB values in a region specified as $-10 < x < 30$ and $2 < y < 40$, with a fixed height of $z = 2$.

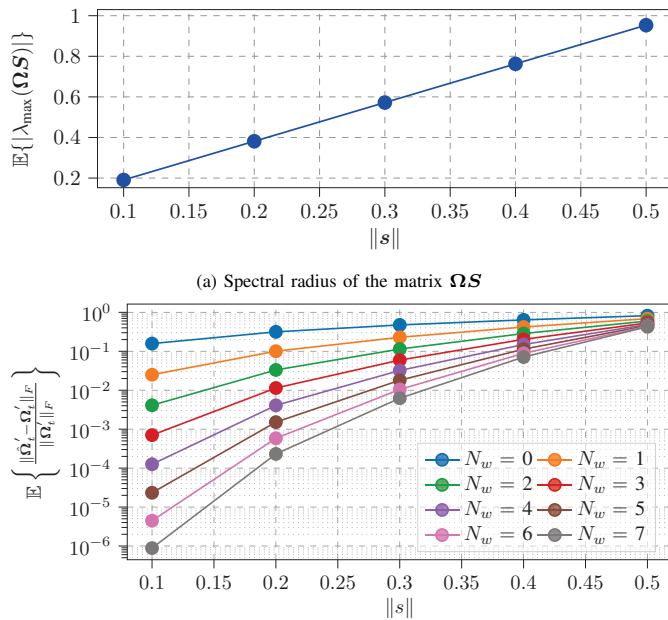
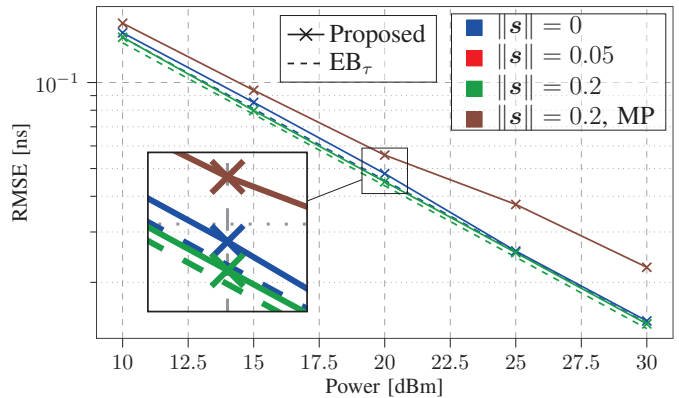


Fig. 5: Validation of Neumann series approximation.

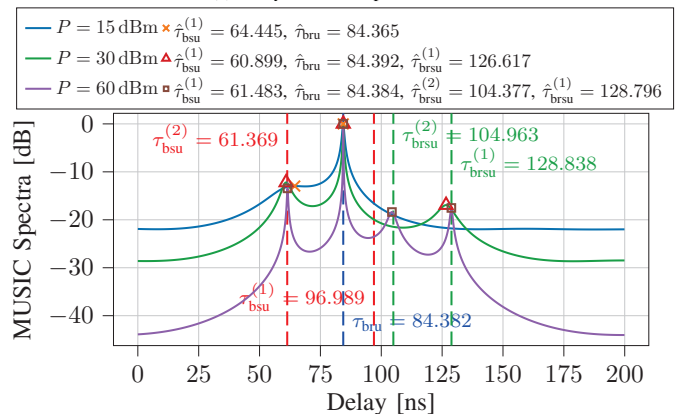
the BS-SP-RIS-UE paths are not detected even at high power. This is due to the fact that these paths, unlike BS-RIS-SP-UE paths, are attenuated by the sharp directive beams of the BS, and secondly, their longer distances compared to the BS-SP-UE paths result in more severe path loss.

2) Positioning and 2D-AOD Estimation Performance:

Fig. 7a and Fig. 7b presents the RMSE for 2D-AOD and 3D localization, respectively. As $\|s\|$ increases, the gap between the classical MC-unaware ML method and the corresponding CRB widens. In contrast, the proposed method closely approaches the CRB, underscoring its superior performance. It is also noteworthy that in the absence of MC (i.e., $\|s\| = 0$), both the MC-unaware ML and the proposed method yield identical results. Moreover, the proposed method remains near the CRB even in the challenging MP environment with $\|s\| = 0.2$. To further evaluate the proposed method against the MC-unaware approach, 2D-AOD RMSE and CRB maps are obtained for various power levels and $\|s\|$ values, as shown in Fig. 8. Notably, the proposed method consistently approaches the CRB values, highlighting its superior effectiveness compared to the MC-unaware approach. However, it can be seen that in Fig. 8b, the proposed method begins to deviate from the CRB values when $\|s\| \geq 0.3$. This performance degradation



(a) Delay estimation performance



(b) MUSIC spectra

Fig. 6: Delay estimation: (a) shows delay estimation RMSE performance versus transmitted power, and (b) depicts MUSIC spectra for three test data with different power $P \in \{15, 30, 60\}$ dBm. Only the detected paths are shown, and the estimated values are depicted in the legend box.

is due to the increasing inaccuracy of the Neumann series approximation at larger $\|s\|$ values, as illustrated in Fig. 5, though the results remain close to the CRB. Additionally, it can be observed that in Fig. 7a and Fig. 8c, for a fixed power, the CRB values decrease slightly with larger $\|s\|$. This is because, as $\|s\|$ increases, the influence of MC on the beampattern becomes more pronounced (see (28)) in presence of noise, slightly enhancing MC estimation accuracy, which in turn improves the estimation of RIS-affected vectors b_n and lowers the CRB. However, as the scattering parameters do not contain position information, this improvement remains marginal.

3) Scattering Parameter Estimation Performance: Fig. 9a presents the RMSE values of the estimated MC coefficients where we have also obtained the results for $\|s\| = 0.05$

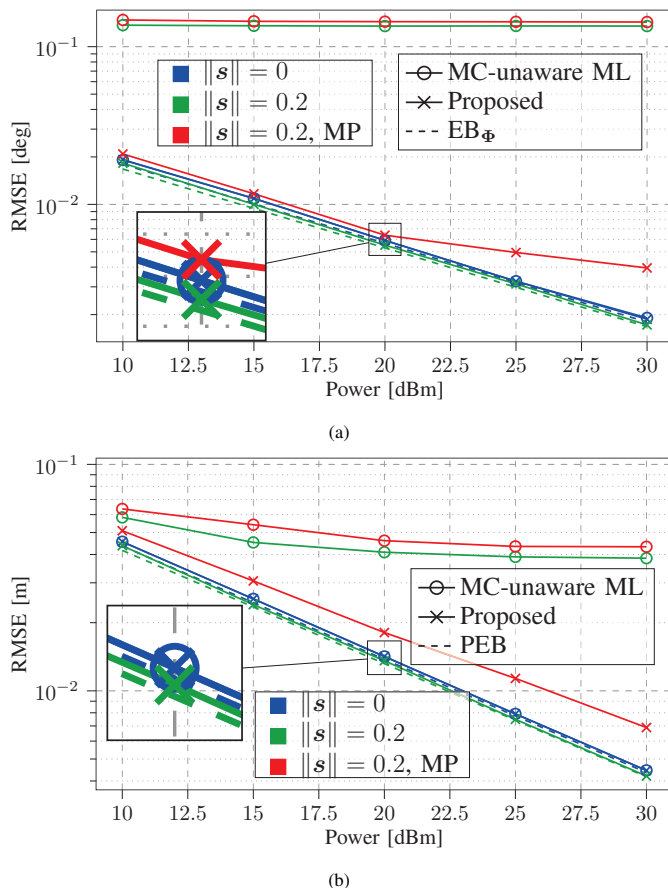


Fig. 7: RMSE performance of the proposed method: (a) 2D-AOD estimation performance; and (b) Localization performance.

for better comparison. It is observed that the performance improves with increasing transmission power. Furthermore, the CRB values exhibit an inverse relationship with $\|s\|$, being higher for smaller $\|s\|$. This can be explained by the fact that for smaller $\|s\|$, the scattering matrix \mathbf{S} in (28) exhibits lower absolute values of the MC terms, which can become negligible compared to noise, complicating MC estimation. While higher $\|s\|$ generally facilitates more accurate MC estimation, the degradation in performance of the classical MC-unaware ML estimator due to MC effects is more pronounced in such cases, compared to scenarios with smaller $\|s\|$.

4) *Impact of Bandwidth in Multipath Scenarios:* Fig. 9b illustrates the RMSE of delay estimation as a function of the number of subcarriers (or equivalently, bandwidth), alongside the optimistic CRB values, which do not account for multipath effects. As expected, increasing the bandwidth enhances delay estimation accuracy. The results show that, despite the presence of multipath, the RMSE closely approaches the CRB computed under no multipath conditions.

E. Impact of Key Parameters on MC Estimation Accuracy

In this subsection, we conduct additional simulations to analyze the impact of some key parameters: number of positions N_u , order of Neumann series used N_w , and $\|s\|$ on MC estimation. In the first experiment, for $N_u = i$, we utilize the first i UE positions $\{\mathbf{p}_{u,i}\}_{j=1}^i$ depicted in Fig. 3b for data generation. The transmitted power is set to $P = 10$ dBm, and the MC vector norm is fixed at $\|s\| = 0.2$. Upon executing the proposed method, we compute the RMSE and the

corresponding CRB values, which are illustrated in Fig. 10a. As anticipated, the MC estimation performance improves with larger values of N_u . Notably, since the CRB for $N_u = i$ is contingent upon the first i positions, the observed improvement is nonlinear.

Notably, since the considered scenario in this paper is in the downlink and the designed codebooks are independent of individual UEs, the proposed methodology can be applied separately at each UE for localization. Furthermore, this experiment can be interpreted as a multi-UE cooperative calibration scenario. As a result, the proposed methodology not only scales efficiently in multi-UE ISAC systems but also benefits from an increased number of UEs, leading to improved localization accuracy and enhanced RIS calibration.

In another experiment, we assess the performance of the proposed method for various values of N_w in terms of $\|s\|$, as illustrated in Fig. 10b. The transmitted power is fixed at $P = 10$ dBm, and the number of positions is set to $N_u = 3$. It is observed that for small values of $\|s\|$, the proposed closed-form coarse estimation and the first-order ($N_w = 1$) Neumann series approximation yield sufficient precision. However, for $\|s\| > 0.1$, the performance of the proposed method with $N_w \in \{1, 2\}$ diverges from the CRB. Therefore, higher values of N_w should be employed for larger $\|s\|$, although this comes at the cost of increased complexity.

VII. CONCLUSION

In this paper, we addressed the challenging problem of 3D localization of a single-antenna UE in the presence of a multi-antenna BS and a UPA-equipped RIS ISAC system in a multipath environment, in presence of MC effects between RIS elements. For the initial 2D-AOD estimation, we developed an efficient MC-unaware ML approach, followed by a closed-form solution for the initial MC estimation. We further proposed an AO-based refinement algorithm to jointly optimize the UE position and MC estimates. Additionally, we extended our method to scenarios where multiple signals from independent UE locations are available, leading to enhanced MC estimation precision. We computed CRB values through FIM analysis to benchmark the proposed approach, and extensive complexity analysis was performed to demonstrate its computational efficiency. Finally, simulation results and CRB comparisons validated the effectiveness and efficiency of the proposed methodology. Here are several avenues for extension of this work, including mobile UEs and examine the combined impact of multiple hardware imperfections, such as RIS pixel failures and amplitude variations.

APPENDIX A

PROOF OF PROPOSITION 1

First, we analyze the convergence properties of the proposed AO based algorithm, which iteratively optimizes the 2D-AODs $\{\psi_{r,u}^{d_n}\}_{n=1}^{N_u}$ via the NM algorithm and the MC vector \mathbf{s} via GD. Let $(\mathbf{s}^{(t)}, \{\psi_{r,u}^{d_n(t)}\}_{n=1}^{N_u})$ denote the updated variables at the t -th iteration of the algorithm, where $t = 0$ corresponds to the initial values. Moreover, in the following, $f(\cdot)$ represents the objective value (27a).

A. Monotonic Increase in the Objective Function

Each iteration of our algorithm consists of two subproblems:

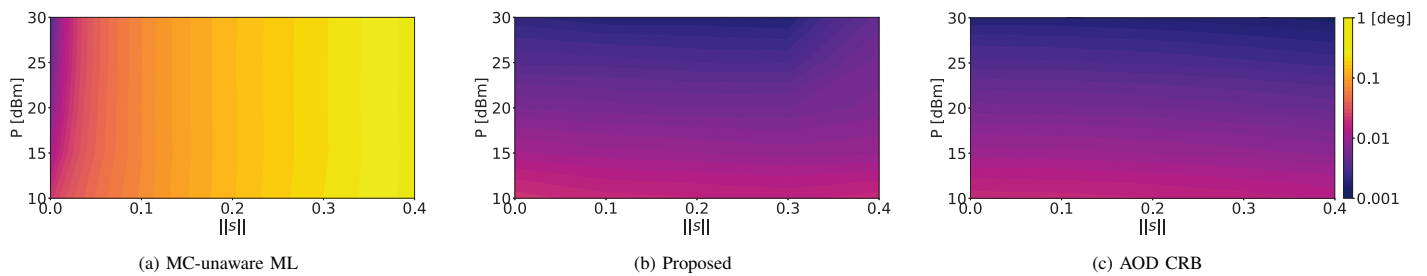


Fig. 8: RMSE comparison of the MC-unaware ML approach with the proposed MC-aware method. The corresponding 2D-AOD CRB heatmap is also plotted as a benchmark.

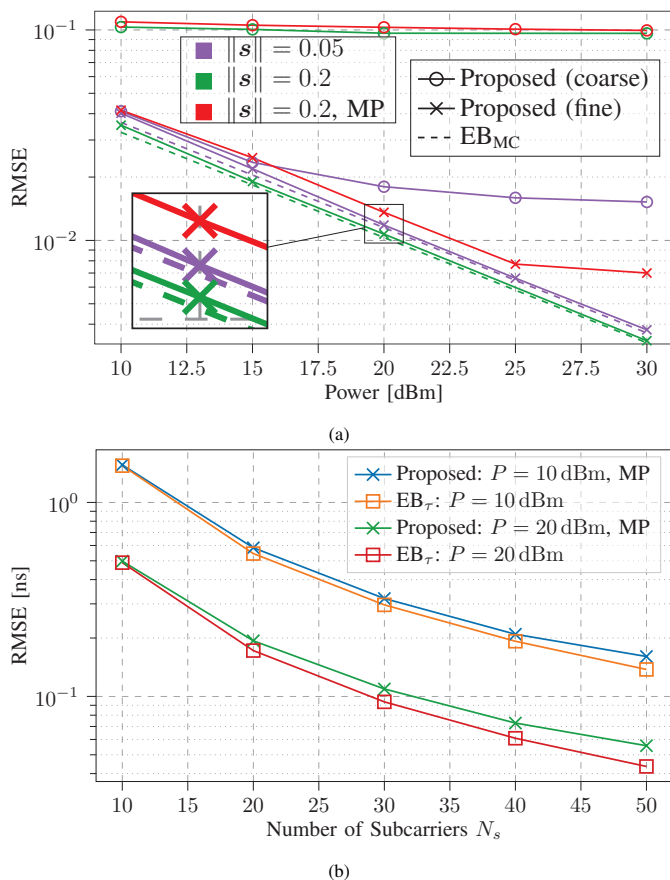


Fig. 9: (a) MC estimation performance.; and (b) Delay estimation under multipath for different subcarrier counts.

- NM for 2D-AOD Optimization:** Given the current value of $\mathbf{s}^{(t)}$, the 2D-AODs $\{\psi_{r,u}^{d_n}\}_{n=1}^{N_u}$ are optimized using the NM algorithm, which is a direct search method that does not require gradient information. Since NM is designed to find a local optimum in non-convex settings and each update ensures a non-decreasing objective value unless a stagnation point⁶ is reached, we obtain $f(\mathbf{s}^{(t)}, \{\psi_{r,u}^{d_n(t+1)}\}_{n=1}^{N_u}) \geq f(\mathbf{s}^{(t)}, \{\psi_{r,u}^{d_n(t)}\}_{n=1}^{N_u})$. It is observed that, due to the sufficiently accurate initialization of the 2D-AODs in (30), the NM algorithm consistently converges to the global optima of this subproblem in all simulations performed in this paper. This observation

⁶A stagnation point in the NM algorithm is reached when it fails to identify better solutions, resulting in nearly identical function values within the simplex, leading to algorithm termination due to the absence of further improvement.

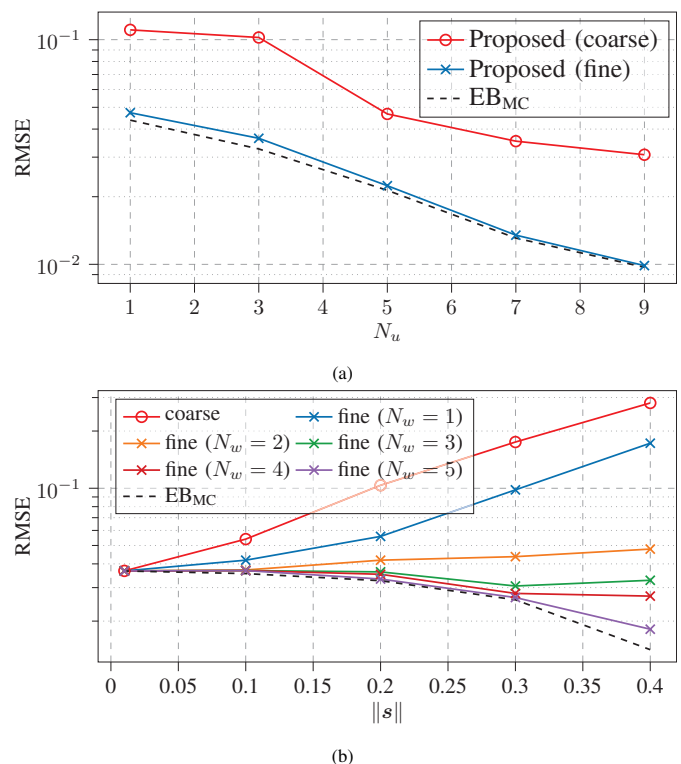


Fig. 10: Impact of key parameters in MC RMSE estimation performance: (a) versus number of UE locations N_u for $\|\mathbf{s}\| = 0.2$. (b) versus $\|\mathbf{s}\|$ for different values of N_w .

aligns with findings in the localization literature (e.g., see [21]). For a detailed mathematical discussion on the convergence properties of low-dimensional NM⁷, we refer the readers to [46].

- GD for \mathbf{s} :** Given the updated 2D-AODs $\{\psi_{r,u}^{d_n(t+1)}\}_{n=1}^{N_u}$, we update \mathbf{s} using gradient descent. Assuming a sufficiently small step size and a smooth, differentiable objective function with respect to \mathbf{s} , gradient descent converges to a stationary point and ensures $f(\mathbf{s}^{(t+1)}, \{\psi_{r,u}^{d_n(t+1)}\}_{n=1}^{N_u}) \geq f(\mathbf{s}^{(t)}, \{\psi_{r,u}^{d_n(t+1)}\}_{n=1}^{N_u})$. Similar to the previous subproblem, in all simulations conducted in this paper, gradient descent converges to the global optima of this subproblem.

Since both steps do not decrease the objective function, the sequence $\{f(\mathbf{s}^{(t)}, \{\psi_{r,u}^{d_n(t)}\}_{n=1}^{N_u})\}$ is monotonically non-decreasing.

⁷Since NM is applied independently to each of the N_u UE positions, the problem dimension in this paper is 2.

We now present a key lemma that will be utilized in the next subsection:

Lemma 1. *The objective function (27a) is upper-bounded.*

Proof. Each term in the summation has the form: $|\mathbf{b}_n^H \hat{\mathbf{y}}_n|^2 / \|\mathbf{b}_n\|^2$. Applying the Cauchy-Schwarz inequality:

$$|\mathbf{b}_n^H \hat{\mathbf{y}}_n|^2 \leq \|\mathbf{b}_n\|^2 \|\hat{\mathbf{y}}_n\|^2 \implies |\mathbf{b}_n^H \hat{\mathbf{y}}_n|^2 / \|\mathbf{b}_n\|^2 \leq \|\hat{\mathbf{y}}_n\|^2 \quad (57)$$

$$\implies f(\mathbf{s}, \{\boldsymbol{\psi}_{r,u}^{d_n}\}_{n=1}^{N_u}) \leq \sum_{n=1}^{N_u} \|\hat{\mathbf{y}}_n\|^2.$$

If we assume that the compressed received signal vectors satisfy $\sum_{n=1}^{N_u} \|\hat{\mathbf{y}}_n\|^2 < \infty$, then the objective function is upper-bounded by this finite value. Hence, the proof is complete.

B. Subsequential Convergence and Stationary Point

Since the objective function is continuous in both \mathbf{s} and $\{\boldsymbol{\psi}_{r,u}^{d_n}\}_{n=1}^{N_u}$, and the updates are designed to lead to non-decreasing objective values, the sequence $f(\mathbf{s}^{(t)}, \{\boldsymbol{\psi}_{r,u}^{d_n(t)}\}_{n=1}^{N_u})$ is monotonically increasing. Furthermore, as the objective function is upper bounded, the *monotone convergence theorem* [47, Theorem 3.3.2] guarantees that the sequence of objective values converges to a finite limit. Under the assumption that the subproblems reach its local optima at each step, any accumulation point $(\mathbf{s}^*, \{\boldsymbol{\psi}_{r,u}^{d_n^*}\}_{n=1}^{N_u})$ must be a stationary point where further optimization does not significantly change the objective function.

Although we proved that Algorithm 1 converges to a stationary point, the non-convex nature of the problem implies that this point may not be globally optimal for any arbitrary initialization. Specifically, the stationary point is highly dependent on the initialization. However, thanks to the sufficiently accurate initial values $(\mathbf{s}^{(0)}, \{\boldsymbol{\psi}_{r,u}^{d_n(0)}\}_{n=1}^{N_u})$ derived in (30) (for 2D-AODs) (37) (for MC vector), the proposed algorithm will have high chances of converging to the global solution.

REFERENCES

- [1] F. Liu, Y. Cui, C. Masouros, J. Xu, T. X. Han, Y. C. Eldar, and S. Buzzi, "Integrated sensing and communications: Toward dual-functional wireless networks for 6G and beyond," *IEEE Journal on Selected Areas in Communications*, vol. 40, no. 6, pp. 1728–1767, 2022.
- [2] K. Zhong, J. Hu, J. Liu, D. An, C. Pan, K. C. Teh, X. Yu, and H. Li, "P2C2M: Parallel product complex circle manifold for RIS-aided ISAC waveform design," *IEEE Transactions on Cognitive Communications and Networking*, vol. 10, no. 4, pp. 1441–1451, 2024.
- [3] J. Zhang, M. Liu, J. Tang, N. Zhao, D. Niyato, and X. Wang, "Joint design for RIS-aided ISAC via deep unfolding learning," *IEEE Transactions on Cognitive Communications and Networking*, pp. 1–1, 2024.
- [4] J. An, H. Li, D. W. K. Ng, and C. Yuen, "Fundamental detection probability vs. achievable rate tradeoff in integrated sensing and communication systems," *IEEE Transactions on Wireless Communications*, vol. 22, no. 12, pp. 9835–9853, 2023.
- [5] Y. Cui, F. Liu, X. Jing, and J. Mu, "Integrating sensing and communications for ubiquitous IoT: Applications, trends, and challenges," *IEEE Network*, vol. 35, no. 5, pp. 158–167, 2021.
- [6] Y. Lin, S. Jin, M. Matthaiou, and X. Yi, "Circular RIS-enabled channel estimation and localization for multi-user ISAC systems," *IEEE Transactions on Wireless Communications*, vol. 23, no. 8, pp. 8730–8743, 2024.
- [7] A. Liu, Z. Huang, M. Li, Y. Wan, W. Li, T. X. Han, C. Liu, R. Du, D. K. P. Tan, J. Lu, Y. Shen, F. Colone, and K. Chetty, "A survey on fundamental limits of integrated sensing and communication," *IEEE Communications Surveys & Tutorials*, vol. 24, no. 2, pp. 994–1034, 2022.
- [8] R. Liu, M. Li, H. Luo, Q. Liu, and A. L. Swindlehurst, "Integrated sensing and communication with reconfigurable intelligent surfaces: Opportunities, applications, and future directions," *IEEE Wireless Communications*, vol. 30, no. 1, pp. 50–57, 2023.
- [9] L. Zhang, X. Lei, T. Ma, H. Niu, and C. Yuen, "Joint user localization, channel estimation, and pilot optimization for RIS-ISAC," *IEEE Transactions on Wireless Communications*, vol. 23, no. 12, pp. 19 302–19 316, 2024.
- [10] J. An, C. Yuen, Y. L. Guan, M. D. Renzo, M. Debbah, H. V. Poor, and L. Hanzo, "Two-dimensional direction-of-arrival estimation using stacked intelligent metasurfaces," *IEEE Journal on Selected Areas in Communications*, vol. 42, no. 10, pp. 2786–2802, 2024.
- [11] J. An, C. Yuen, C. Xu, H. Li, D. W. K. Ng, M. Di Renzo, M. Debbah, and L. Hanzo, "Stacked intelligent metasurface-aided mimo transceiver design," *IEEE Wireless Communications*, vol. 31, no. 4, pp. 123–131, 2024.
- [12] H. Niu, J. An, A. Papazafeiropoulos, L. Gan, S. Chatzinotas, and M. Debbah, "Stacked intelligent metasurfaces for integrated sensing and communications," *IEEE Wireless Communications Letters*, vol. 13, no. 10, pp. 2807–2811, 2024.
- [13] A. Fadakar, A. Mansourian, and S. Akhavan, "Deep learning aided multi-source passive 3D AOA wireless positioning using a moving receiver: A low complexity approach," *Ad Hoc Networks*, vol. 154, p. 103382, 2024.
- [14] A. Mansourian, A. Fadakar, S. Akhavan, and B. Maham, "Robust 3D multi-source localization with a movable antenna array via sparse signal processing," *IEEE Open Journal of the Communications Society*, pp. 1–1, 2025.
- [15] A. Mansourian, A. Fadakar, and S. Akhavan, "Enhanced K-SVD based approach for multi-source 3D localization with a mobile receiver," in *2024 IEEE 100th Vehicular Technology Conference (VTC2024-Fall)*, 2024, pp. 1–5.
- [16] H. Chen, P. Zheng, M. F. Keskin, T. Al-Naffouri, and H. Wymeersch, "Multi-RIS-enabled 3D sidelink positioning," *IEEE Transactions on Wireless Communications*, vol. 23, no. 8, pp. 8700–8716, 2024.
- [17] H. Chen, H. Sarrieddeen, T. Ballal, H. Wymeersch, M.-S. Alouini, and T. Y. Al-Naffouri, "A tutorial on terahertz-band localization for 6G communication systems," *IEEE Communications Surveys & Tutorials*, vol. 24, no. 3, pp. 1780–1815, 2022.
- [18] A. Fadakar, M. Sabbaghian, and H. Wymeersch, "Multi-RIS-assisted 3D localization and synchronization via deep learning," *IEEE Open Journal of the Communications Society*, vol. 5, pp. 3299–3314, 2024.
- [19] C. Ozturk, M. F. Keskin, V. Sciancalepore, H. Wymeersch, and S. Gezici, "RIS-aided localization under pixel failures," *IEEE Transactions on Wireless Communications*, vol. 23, no. 8, pp. 8314–8329, 2024.
- [20] J. He, A. Fakhreddine, C. Vanwynsberghe, H. Wymeersch, and G. C. Alexandropoulos, "3D localization with a single partially-connected receiving RIS: Positioning error analysis and algorithmic design," *IEEE Transactions on Vehicular Technology*, vol. 72, no. 10, pp. 13 190–13 202, 2023.
- [21] A. Fascista, M. F. Keskin, A. Coluccia, H. Wymeersch, and G. Seco-Granados, "RIS-aided joint localization and synchronization with a single-antenna receiver: Beamforming design and low-complexity estimation," *IEEE Journal of Selected Topics in Signal Processing*, vol. 16, no. 5, pp. 1141–1156, 2022.
- [22] M. Di Renzo, F. H. Danufane, and S. Tretyakov, "Communication models for reconfigurable intelligent surfaces: From surface electromagnetics to wireless networks optimization," *Proceedings of the IEEE*, vol. 110, no. 9, pp. 1164–1209, 2022.
- [23] P. Zheng, R. Wang, A. Shamim, and T. Y. Al-Naffouri, "Mutual coupling in RIS-aided communication: Model training and experimental validation," *IEEE Transactions on Wireless Communications*, vol. 23, no. 11, pp. 17 174–17 188, 2024.
- [24] M. Bayraktar, N. González-Prelcic, G. C. Alexandropoulos, and H. Chen, "RIS-aided joint channel estimation and localization at mmwave under hardware impairments: A dictionary learning-based approach," *IEEE Transactions on Wireless Communications*, vol. 23, no. 12, pp. 19 696–19 712, 2024.
- [25] Z.-M. Liu, C. Zhang, and S. Y. Philip, "Direction-of-arrival estimation based on deep neural networks with robustness to array imperfections," *IEEE Transactions on Antennas and Propagation*, vol. 66, no. 12, pp. 7315–7327, 2018.
- [26] H. Chen, M. F. Keskin, S. R. Aghdam, H. Kim, S. Lindberg, A. Wolfgang, T. E. Abruđan, T. Eriksson, and H. Wymeersch, "Modeling and analysis of OFDM-based 5G/6G localization under hardware impairments," *IEEE Transactions on Wireless Communications*, vol. 23, no. 7, pp. 7319–7333, 2024.
- [27] R. Faqiri, C. Saigre-Tardif, G. C. Alexandropoulos, N. Shlezinger, M. F. Imani, and P. del Hougne, "Physfad: Physics-based end-to-end channel modeling of RIS-parametrized environments with adjustable fading," *IEEE Transactions on Wireless Communications*, vol. 22, no. 1, pp. 580–

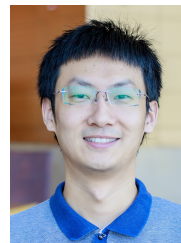
- 595, 2023.
- [28] G. Gradoni and M. Di Renzo, "End-to-end mutual coupling aware communication model for reconfigurable intelligent surfaces: An electromagnetic-compliant approach based on mutual impedances," *IEEE Wireless Communications Letters*, vol. 10, no. 5, pp. 938–942, 2021.
- [29] S. Shen, B. Clerckx, and R. Murch, "Modeling and architecture design of reconfigurable intelligent surfaces using scattering parameter network analysis," *IEEE Transactions on Wireless Communications*, vol. 21, no. 2, pp. 1229–1243, 2022.
- [30] H. Li, S. Shen, M. Nerini, M. Di Renzo, and B. Clerckx, "Beyond diagonal reconfigurable intelligent surfaces with mutual coupling: Modeling and optimization," *IEEE Communications Letters*, vol. 28, no. 4, pp. 937–941, 2024.
- [31] D. Wijekoon, A. Mezghani, and E. Hossain, "Phase shifter optimization in RIS-aided MIMO systems under multiple reflections," *IEEE Transactions on Wireless Communications*, vol. 23, no. 8, pp. 8969–8983, 2024.
- [32] S. Rivetti, J. Miguel Mateos-Ramos, Y. Wu, J. Song, M. F. Keskin, V. Yajnanarayana, C. Häger, and H. Wymeersch, "Spatial signal design for positioning via end-to-end learning," *IEEE Wireless Communications Letters*, vol. 12, no. 3, pp. 525–529, 2023.
- [33] P. Zheng, S. Tarboush, H. Sameddeen, and T. Y. Al-Naffouri, "Mutual coupling-aware channel estimation and beamforming for RIS-assisted communications," 2024. [Online]. Available: <https://arxiv.org/abs/2410.04110>
- [34] A. Abrardo, A. Toccafondi, and M. Di Renzo, "Design of reconfigurable intelligent surfaces by using S-parameter multiport network theory—optimization and full-wave validation," *IEEE Transactions on Wireless Communications*, vol. 23, no. 11, pp. 17 084–17 102, 2024.
- [35] F. Shi, W. Li, C. Tang, Y. Fang, P. V. Brennan, and K. Chetty, "Decimeter-level indoor localization using WiFi round-trip phase and factor graph optimization," *IEEE Journal on Selected Areas in Communications*, vol. 42, no. 1, pp. 177–191, 2024.
- [36] W. Wang and W. Zhang, "Joint beam training and positioning for intelligent reflecting surfaces assisted millimeter wave communications," *IEEE Transactions on Wireless Communications*, vol. 20, no. 10, pp. 6282–6297, 2021.
- [37] J. An, C. Xu, Q. Wu, D. W. K. Ng, M. Di Renzo, C. Yuen, and L. Hanzo, "Codebook-based solutions for reconfigurable intelligent surfaces and their open challenges," *IEEE Wireless Communications*, vol. 31, no. 2, pp. 134–141, 2024.
- [38] H. Kim, H. Chen, M. F. Keskin, Y. Ge, K. Keykhosravi, G. C. Alexandropoulos, S. Kim, and H. Wymeersch, "RIS-enabled and access-point-free simultaneous radio localization and mapping," *IEEE Transactions on Wireless Communications*, vol. 23, no. 4, pp. 3344–3360, 2024.
- [39] A. Fadakar, A. Jafari, and S. Akhavan, "Multi-source 2D-AOA estimation via deep learning," in *2024 IEEE 100th Vehicular Technology Conference (VTC2024-Fall)*, 2024, pp. 1–5.
- [40] A. Fadakar, A. Mansourian, and S. Akhavan, "Localization using convolutional neural networks with mobile array," in *2024 IEEE 100th Vehicular Technology Conference (VTC2024-Fall)*, 2024, pp. 1–5.
- [41] M. F. Keskin, H. Wymeersch, and V. Koivunen, "MIMO-OFDM joint radar-communications: Is ICI friend or foe?" *IEEE Journal of Selected Topics in Signal Processing*, vol. 15, no. 6, pp. 1393–1408, 2021.
- [42] K. Lee *et al.*, "Deep learning-aided coherent direction-of-arrival estimation with the FTMR algorithm," *IEEE Transactions on Signal Processing*, vol. 70, pp. 1118–1130, 2022.
- [43] A. Fadakar, A. Jafari, P. Tavana, R. Jahani, and S. Akhavan, "Deep learning based 2D-DOA estimation using I-shaped arrays," *Journal of the Franklin Institute*, vol. 361, no. 6, p. 106743, 2024.
- [44] Z. Muhi-Eldeen, L. Ivrisimtzis, and M. Al-Nuaimi, "Modelling and measurements of millimetre wavelength propagation in urban environments," *IET microwaves, antennas & propagation*, vol. 4, no. 9, pp. 1300–1309, 2010.
- [45] S. Theodoridis and R. Chellappa, *Academic Press library in signal processing: communications and signal processing*. Academic Press, 2013.
- [46] J. C. Lagarias, J. A. Reeds, M. H. Wright, and P. E. Wright, "Convergence properties of the nelder–mead simplex method in low dimensions," *SIAM Journal on Optimization*, vol. 9, no. 1, pp. 112–147, 1998.
- [47] R. G. Bartle and D. R. Sherbert, *Introduction to real analysis*. Wiley New York, 2000, vol. 2.



Alireza Fadakar (S'25) received the B.Sc. and M.Sc. degrees in electrical engineering from the University of Tehran, Tehran, Iran, in 2020 and 2023, respectively. In January 2025, he joined the Ming Hsieh Department of Electrical and Computer Engineering at the University of Southern California as a Ph.D. student. He is a recipient of the USC Annenberg Fellowship. In 2015, he was awarded a silver medal in the Iranian National Mathematics Olympiad. His research interests include wireless communications, signal processing, localization, channel estimation, integrated sensing and communication, cognitive radio, as well as the application of machine learning in these areas.



Musa Furkan Keskin (M'20) received the Ph.D. degree in Electrical and Electronics Engineering from Bilkent University, Ankara, Turkey, in 2018. He is currently a Research Specialist in the Department of Electrical Engineering at Chalmers University of Technology in Gothenburg, Sweden, where he is leading and contributing to various interdisciplinary and industry-focused research projects at both Swedish and European levels, with a specialization in integrated localization, communication and sensing in 6G systems. His awards include the 2019 IEEE Turkey Best Ph.D. Thesis Award for his work on visible light positioning systems, the EU MSCA Postdoctoral Fellowship for his project "OTFS-RADCOM: A New Waveform for Joint Radar and Communications Beyond 5G.", and the Swedish Research Council (VR) Starting Grant for his project on "Localization and Sensing for Perceptive Cell-Free Networks Towards 6G". Dr. Keskin serves as an Editor for the IEEE Transactions on Communications and IEEE Transactions on Mobile Computing.



Hui Chen (S'18-M'21) received the Ph.D. Degree in Electrical and Computer Engineering from King Abdullah University of Science and Technology (KAUST), Saudi Arabia, in 2021. He is currently a Research Specialist at Chalmers University of Technology, Sweden. He is actively contributing to several EU projects (e.g., 6G-DISAC, HEXA-X), Swedish Vinnova, and VR projects in the field of localization and sensing. He is the recipient of the European Union Marie Skłodowska-Curie Postdoctoral Fellowship (MSCA-PF), the Swedish Vinnova International Mobility Grant, Chalmers Area-of-Advance Transport/ICT Seed Fundings, and the Ericsson Research Grant. His research focuses on 5G/6G localization and sensing, distributed ISAC, and machine learning.



Henk Wymeersch (S'01, M'05, SM'19, F'24) obtained the Ph.D. degree in Electrical Engineering/Applied Sciences in 2005 from Ghent University, Belgium. He is currently a Professor of Communication Systems with the Department of Electrical Engineering at Chalmers University of Technology, Sweden. Prior to joining Chalmers, he was a post-doctoral researcher from 2005 until 2009 with the Laboratory for Information and Decision Systems at the Massachusetts Institute of Technology. Prof. Wymeersch served as Associate Editor for IEEE Communication Letters, IEEE Transactions on Wireless Communications, and IEEE Transactions on Communications and is currently Senior Member of the IEEE Signal Processing Magazine Editorial Board. During 2019-2021, he was an IEEE Distinguished Lecturer with the Vehicular Technology Society. His current research interests include the convergence of communication and sensing, in a 5G and Beyond 5G context.